Journal Pre-proofs

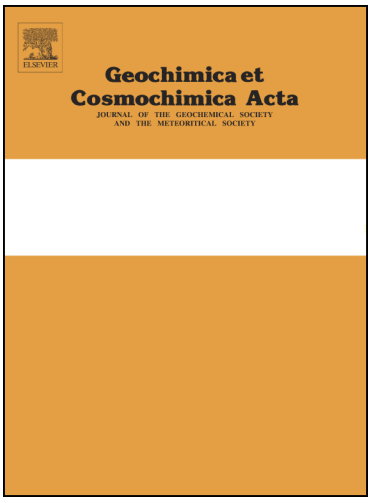

Barium isotope composition of depleted MORB mantle constrained by basalts from the South Mid-Atlantic Ridge (5–11°S) with implication for recycled components in the convecting upper mantle

Fei Wu, Simon Turner, Kaj Hoernle, Folkmar Hauff, Bruce F. Schaefer, Thomas Kokfelt, Ilya Bindeman

PII: S0016-7037(22)00620-2
DOI: https://doi.org/10.1016/j.gca.2022.11.013
Reference: GCA 12871

To appear in: *Geochimica et Cosmochimica Acta*

Received Date: 7 May 2022
Revised Date: 30 October 2022
Accepted Date: 14 November 2022

Please cite this article as: Wu, F., Turner, S., Hoernle, K., Hauff, F., Schaefer, B.F., Kokfelt, T., Bindeman, I., Barium isotope composition of depleted MORB mantle constrained by basalts from the South Mid-Atlantic Ridge (5–11°S) with implication for recycled components in the convecting upper mantle, *Geochimica et Cosmochimica Acta* (2022), doi: https://doi.org/10.1016/j.gca.2022.11.013

Barium isotope composition of depleted MORB mantle constrained by basalts from the South Mid-Atlantic Ridge (5–11°S) with implication for recycled components in the convecting upper mantle

Fei Wu[a,b*], Simon Turner[b], Kaj Hoernle[c,d], Folkmar Hauff[c], Bruce F. Schaefer[b], Thomas Kokfelt[e], Ilya Bindeman[f]

[a] School of Earth Sciences, State Key Laboratory of Geological Processes and Mineral Resources, China University of Geosciences, Wuhan 430074, China

[b] Department of Earth and Environmental Sciences, Macquarie University, Sydney, NSW 2109, Australia

[c] GEOMAR Helmholtz Centre for Ocean Research Kiel, 24148 Kiel, Germany

[d] Institute of Geosciences, Kiel University, 24118 Kiel, Germany

[e]GEUS, Department of Petrology and Economic Geology, ØsterVoldgade 10, 1350, Copenhagen, Denmark

[f]Department of Earth Sciences, 1275 University of Oregon Eugene, OR 97403, USA

*corresponding author: E-mail address: wufei@cug.edu.cn (Fei Wu)

Abstract

Stable barium (Ba) isotopes are emerging as tracers for the recycling of crustal material into the mantle. Small but significant Ba isotope variations have been found in global MORB ($\delta^{138/134}$Ba values of -0.04‰ to 0.15‰), but the processes causing these Ba isotope variations remain poorly understood. In addition, uncertainties still exist in the estimate of the Ba isotope composition of the depleted upper mantle. Here, we present a systematic study of Ba isotopes for well-characterized MORB glass samples from the South Mid-Atlantic Ridge (SMAR) between 5 and 11°S, which span a wide range of radiogenic isotope ratios and trace element contents. Our results show that the northernmost segment A0 basalts with highly depleted radiogenic isotope compositions have $\delta^{138/134}$Ba values ranging from -0.02 to 0.05‰. In comparison, the $\delta^{138/134}$Ba values of the isotopically enriched basalts from the A1-A4 segments vary from 0.02 to 0.11‰. Thus, while small, the enriched components involved can be observed to modify the Ba isotope composition of the mantle source beneath A1-A4 segments. Combining our new measurements with literature data, this study places new constraints on the Ba isotope composition of the depleted upper mantle, as well as the origin of Ba isotope heterogeneity in MORB. The Ba isotope composition of the depleted upper mantle in the absence of recycled components is estimated to have a $\delta^{138/134}$Ba value of 0.03 to 0.05‰, which can be adopted as the baseline for using Ba isotope ratios as a tracer of mass transfer processes between the crust and mantle. In comparison, global MORB have $\delta^{138/134}$Ba values ranging from -0.04‰ to 0.15‰. No global correlation is observed between Ba isotope ratios and geochemical parameters that record mantle enrichment, indicating that the Ba isotope variations in MORB cannot be simply ascribed to the addition of some single component, such as sediment. Models for melting and mixing between recycled materials and depleted mantle suggest that the variable Ba isotope compositions of the enriched MORB require a contribution from recycled altered oceanic crust and crustal sedimentary materials. Therefore, these recycled components both play important roles in the chemical budget of the convecting upper mantle, especially for incompatible elements such as Ba.

Key words: Ba isotope; mid-ocean-ridge basalt; South Atlantic Ocean; depleted upper mantle; mantle heterogeneity

1. Introduction

Partial melting of the mantle is the main cause of chemical differentiation of the silicate Earth via generation of oceanic and continental crust (e.g., Allègre et al., 1987; Hofmann, 1988). Elements with high incompatibility in mantle minerals are preferentially extracted by low-degree partial melts, resulting in incompatible element depletion in the residual, depleted mantle (e.g., Hofmann, 1988). This depleted mantle is continuously re-enriched by the subduction of crustal materials, leading to large-scale heterogeneity. The chemical and isotopic variability observed in oceanic island basalts (OIBs) (e.g., Hofmann, 2007; Jackson and Dasgupta, 2008) and mid-ocean ridge basalts (MORB) (e.g., Klein and Langmuir, 1987; Arevalo and McDonough, 2010; Gale et al., 2013) reflect the compositional heterogeneity of the mantle driven by such crust-mantle interaction (Stracke, 2012). The origin of isotopically distinct reservoirs in the mantle remains enigmatic (e.g., Zindler and Hart, 1986; Rampone and Hofmann, 2012; White, 2015; Hofmann, 2014). The emergence of new tracers that have the ability to quantify the relative contribution of specific recycled components affords new perspectives on the geodynamic process that causes mantle heterogeneity.

Barium (Ba) is highly incompatible during mantle melting and is accordingly much more enriched in the continental crust (Rudnick and Gao, 2014) and marine sediments (Plank and Langmuir, 1998) than in the mantle (Workman and Hart, 2005). Barium is also a fluid-mobile element that has been widely used to trace slab-derived fluids in subduction zones (e.g., Zack et al., 2001; Kessel et al., 2005; Bebout, 2014). The prominent Ba enrichments observed in ocean island basalts (OIBs), arc rocks, mantle rocks and some MORB might reflect low-degree mantle melting, addition of recycled crustal materials with high Ba enrichments, and/or melting of mantle metasomatized by melts/fluids derived from variable sources. Ba isotope studies of seawater (e.g., Horner et al., 2015; Hsieh and Henderson, 2017), river water (e.g., Gou et al., 2020), marine sediments (Bridgestock et al., 2018; Nielsen et al., 2020), coral and sedimentary carbonates (e.g., Pretet et al., 2016; Wei et al., 2021; Zhang et al., 2022), granite (Deng et al., 2021, 2022; Huang et al., 2021), altered oceanic crust (Nielsen et al., 2020), and upper continental rocks (Nan et al., 2018) have shown that these materials experience surficial low-temperature chemical modification and exhibit strong Ba isotopic heterogeneity. For comparison, mantle melting is known to induce little if any Ba isotope fractionation (e.g., Nielsen et al., 2018;

Nan et al., 2022). Accordingly, Ba isotopes have been applied to trace the recycling of crustal material in mantle-derived igneous rocks including MORB (Nielsen et al., 2018; Nan et al., 2022), active and ancient arc magmas (Nielsen et al., 2020; Wu et al., 2020; Hao et al., 2022), ocean island basalts (Bai et al., 2022; Yu et al., 2022), and continental basalts (Zhao et al., 2021; Xu et al., 2022; Dong et al., 2022).

Small but significant Ba isotope variations have been observed in MORB, and these were originally ascribed to mixing between depleted MORB melts characterized by $\delta^{138/134}$Ba ~0.14‰ and enriched MORB melts characterized by $\delta^{138/134}$Ba ~0.03‰ ($\delta^{138/134}Ba = [(^{138}Ba/^{134}Ba)_{sample}/(^{138}Ba/^{134}Ba)_{SRM3104a} - 1] \times 1000‰$) (Nielsen et al., 2018). This might indicate the addition of sediment-rich material with isotopically light Ba to the upper mantle, and the upper mantle is further proposed to be pervasively contaminated by a minor amount of sediment (Nielsen et al., 2018). Notably, the most depleted MORB samples studied by Nielsen et al. (2018) show significant Ba isotope variations ($\delta^{138/134}$Ba from 0.03‰ to 0.14‰) despite their limited variations in $^{87}Sr/^{86}Sr$ (0.70230 to 0.70245) and $^{143}Nd/^{144}Nd$ (0.51315 to 0.51322). More scattered $\delta^{138/134}$Ba variation in MORB were observed by Nan et al. (2022), who argued against the simply binary mixing relationship between Ba isotopes and other indicators of mantle enrichment suggested by Nielsen et al. (2018).

Nielsen et al. (2018) also proposed that the depleted upper mantle is characterized by $\delta^{138/134}$Ba ~0.14‰. This was used as the reference value for investigations of arc lavas from the Aleutian and Ryukyu arcs (Nielsen et al., 2020) and continental basalts in eastern China (Xu et al., 2022). Mantle-derived carbonatites have limited Ba isotope variations with average $\delta^{138/134}$Ba values of ~0.05‰ (Li et al., 2019), implying a contribution of isotopically light, recycled sediments if the depleted upper mantle is characterized by $\delta^{138/134}$Ba ~0.14‰. Alternatively, it might be that the convective upper mantle is characterized by $\delta^{138/134}$Ba ~0.05‰ (Li et al., 2019; Nan et al., 2022), and this was taken as the reference value to constrain the relative importance of different slab inputs in Tonga-Kermadec arc lavas (Wu et al., 2020). Clearly, it is critical to better constrain the Ba isotope composition of the depleted upper mantle.

In this study, we present new Ba isotope ratios for 30 well-characterized MORB sampled along the Southern Mid-Atlantic Ridge (SMAR) between 5 and 11°S (Fig. 1) and from nearby seamounts. They have large trace element (e.g., $(La/Sm)_N$ from 0.3 to 2.5, normalized to

primitive mantle, Sun and McDonough, 1989) and radiogenic isotope (e.g., $^{87}Sr/^{86}Sr$ from 0.70211 to 0.70273, $^{143}Nd/^{144}Nd$ from 0.51333 to 0.51300) variations that encompass a significant proportion of the variation in global MORB. New Hf and O isotope data are also presented to further identify source heterogeneity and evaluate the potential effect of alteration and assimilation on these basalts. Our new results, together with published data, further constrain the origin of Ba isotopic heterogeneity in MORB, and provide a new benchmark for the Ba isotope composition of the depleted upper mantle.

2. Geological background and sample selection

The SMAR between the Ascension Fracture Zone (AFZ, 7°30′S) and the Bode Verde Fracture Zone (BVFZ, 11°30′S; Fig. 1) can be divided into five segments, based on non-transform discontinuities along the ridge axis. Segments are numbered A0 to A4 going southward from the AFZ to the BVFZ (Fig. 1B). All samples between 4.8°S and 7.6°S are referred to as the A0 group, which includes the northernmost sample location of segment A1 (130DS), a small segment within the AFZ and all samples north of the AFZ. Water depths to the ridge axis for the A0, A1 and A4 sample locations are >2950 m below sea level and these portions are characterized by deep rift valleys, typical of slow spreading centers. In contrast, segments A2 (2100–3000 m below sea level) and A3 (~1400–3000 m below sea level) are characterized by rifted axial highs, typical of fast spreading ridges (Bruguier et al., 2003). The decreasing depth of the ridge axis correlates with crustal thickness and seafloor morphology, with the thickness increasing from normal (~6 km) at segments A1 and A4 to ~11 km near a seamount chain extending from the A3 ridge axis to the east (Minshull et al., 1998; Bruguier et al., 2003). Despite the proximity of Ascension Island to the central part of the A1 ridge axis (~80 km) and the presence of an Ascension geochemical signature in the segment A1 lavas (see below), the depths and morphology of this segment are typical of the SMAR farther north. The full spreading rate along the SMAR between the AFZ and BVFZ is 32–33 mm/yr (DeMets et al., 1994). Bathymetric data indicate that the A2 ridge segment has been propagating north for at least the last 4 Ma (Bruguier et al., 2003), while combined bathymetric and magnetic data indicate that the A3 ridge segment experienced an eastward jump 1–2 Ma ago (Brozena, 1986; Bruguier et al., 2003).

The basalts from SMAR between the AFZ and BVFZ have SiO_2 = 46.2–52.3 wt.% and MgO = 9.7–3.9 wt.% (Möller, 2002; Hoernle et al., 2011; Turner et al., 2015). Those from segment A0, including the AFZ samples, have low $(La/Sm)_N$ of 0.3-0.7. In contrast, the basalts from segment A3 (ridge and seamounts) have high $(La/Sm)_N$ of 1.3-2.5, which are the typical features of E-MORB and ocean island basalt (OIB) type lavas. The basalts from segments A2 and A4 have $(La/Sm)_N$ ratios between those from segments A1 and A3. The basalts from segment A1 show large $(La/Sm)_N$ variations ranging from 0.5 to 2.2 (Fig. S1). The variable $(La/Sm)_N$ ratios as well as the radiogenic isotope variations in the basalts along the ridge record heterogeneity in their source regions (Fig. S1) (Paulick et al., 2010; Hoernle et al., 2011). Almeev et al. (2007) determined that the H_2O contents in the parental melts for these basalts with a typical depleted character were low (0.04–0.09 wt.%), whereas those containing a contribution from enriched components were significantly higher (0.30–0.55 wt.%).

Hoernle et al. (2011) used a plot of $^{143}Nd/^{144}Nd$ versus $^{208}Pb/^{206}Pb$ (reproduced here in Fig. S1) to argue that the SMAR basalts sampled one depleted and three enriched end-member components as follows: the depleted MORB source component (DMM) is sampled at segment A0 (including the AFZ samples); segment A1 basalts extend from the depleted component to an Ascension Island-like, enriched component; segment A2 basalts extend from the depleted component toward an enriched component with higher $^{143}Nd/^{144}Nd$ and $^{208}Pb/^{206}Pb$ than the inferred Ascension Island end-member; the basalts from segments A3 + A4 extend from the depleted component toward an enriched component that has lower $^{143}Nd/^{144}Nd$ than the inferred Ascension Island end-member (see Fig. S1). It is notable that the depleted component sampled from segment A0 represents the most depleted composition sampled thus far along the mid-Atlantic ridge (Hoernle et al., 2011; Urann et al., 2020). For comparison, Hf-Nd isotope relationships of the same area were suggested by Paulick et al. (2010) to reflect mixing between two separate depleted end-member components and a single, enriched, Ascension Island-like endmember. Turner et al. (2015) used U-series disequilibria to suggest that the basalts may be mixtures between partial melts of spinel peridotite and a recycled mafic lithology (pyroxenite or eclogite).

The samples selected for whole rock Ba isotope analyses were aliquots of the same glasses for which trace element and Sr–Nd–Pb isotope data were presented by Hoernle et al. (2011) and

Turner et al. (2015). We chose 6 samples from the A0 and AFZ segments, 6 from segment A1, 6 from segment A2, 2 from segment A3, 4 from the A3 seamount and 6 from segment A4. The chosen samples encompass the entire geochemical spectra observed along the SMAR between the AFZ and BVFZ (Fig. S1).

3. Analytical methods

3.1. Oxygen isotope analyses

Oxygen isotope analyses were performed at the University of Oregon stable isotope laboratory. Oxygen isotope measurements for $\delta^{18}O$ relied on 1 to 1.5 mg of material, predominantly single chips of glass, and were performed by laser fluorination and gas-source mass spectrometry (MAT253). We used purified BrF_5 as a reagent and a Hg diffusion pump to clean the excess F_2 gas, then converted purified O_2 into CO_2 and analyzed it in a dual inlet mode on the MAT253 mass spectrometer integrated with the vacuum line, as this method is most precise for $\delta^{18}O$ determination (e.g., Bindeman, 2008). Sample yields were measured in a calibrated volume using a Baratron gauge. San Carlos Olivine ($\delta^{18}O$ = 5.25‰), UWG2 garnet ($\delta^{18}O$ = 5.80‰, Valley et al. 1995) and an in house UOG garnet standard ($\delta^{18}O$=6.52‰) calibrated relative to the other two were used to calibrate the data on the VSMOW scale. Each session included analyses of 4 to 6 standards, and correction for day-to-day variability was 0 to 0.2‰. CO_2 gas was used as a working standard and was periodically rerun against OZTECH CO_2 gas. Errors for standards in individual sessions ranged from ±0 to ±0.11‰ and were conservatively estimated to be ±0.1‰.

3.2. Hafnium isotope analyses

Radiogenic Hf isotope analyses were conducted at the GEOMAR Helmholtz Centre for Ocean Research Kiel, Germany. Hf ion chromatography followed the established standard procedures of Geldmacher et al. (2006). Purified samples were analyzed on a Nu-Plasma II MC-ICP-MS in standard bracketing mode. Our in-house SPEX CertiPrep Hf solution (Lot #9) gave $^{176}Hf/^{177}Hf$ = 0.282170 ± 0.000006 (n= 54), corresponding to $^{176}Hf/^{177}Hf$ = 0.282163 for JMC475 (Blichert-Toft et al., 1997). Total chemistry blanks were <100 pg for Hf and therefore considered negligible relative to the amount of Hf used (200-800 ng).

3.3. Barium isotope analyses

The sample preparation for Ba isotope measurement was conducted at the Macquarie University – Thermo Scientific Isotope Development Laboratories (Australia). Suitable glasses were crushed to 0.5–1 mm sized chips in an agate mortar and pestle, washed in deionized water and hand-picked under a binocular microscope to avoid visible evidence for crystals, vesicles, hydrothermal alteration and/or Mn coatings. Selected glass chips were further ultrasonicated in deionized water for 20 min and rinsed twice with deionized water. Suitable amounts of washed glass chips containing approximately 0.2–1 μg Ba were weighted and equilibrated with an appropriate amount of ^{135}Ba–^{136}Ba double spike. After total decomposition in a 1:2 (v/v) mixture of concentrated HF and HNO_3, the residues were dried down and fluxed with 6 mol L^{-1} HCl. Finally, the samples were dissolved in 1 mL of 3 mol L^{-1} HCl.

Separation of Ba from the sample matrix used a procedure modified from Nan et al. (2015). Briefly, Ba was isolated by being passed twice through columns filled with AG50W-X12 (200–400 mesh, Bio-Rad, USA) cation exchange resin. The samples were loaded and washed with 3 mol L^{-1} HCl to elute the matrix elements. Barium was then collected with 3 mol L^{-1} HNO_3. The Ba cut was dried and dissolved in 2% HNO_3 (m/m) ready for instrument analysis.

Barium isotope measurements were performed using a Thermo Scientific Neptune plus MC-ICP-MS with instrumental mass bias corrected using the ^{135}Ba–^{136}Ba double spike (Wu et al., 2020). ^{134}Ba, ^{135}Ba, ^{136}Ba, and ^{138}Ba were used in the double-spike inversion. The signal intensities of ^{131}Xe, ^{139}La, and ^{140}Ce were monitored to correct for isobaric interferences on ^{134}Ba, ^{136}Ba, and ^{138}Ba. The baseline was measured in 2% HNO_3 (m/m) prior to each sample for on-peak background subtraction. Each sample was typically analyzed at least three times. This procedure achieved 2SD uncertainties of ~0.02–0.04‰, similar to the long-term external 2SD reproducibility of ±0.04‰ based on replicate measurements of in-house solution standards and USGS reference materials (Table 1) (Wu et al., 2020).

4. Results

The barium, oxygen and hafnium isotope compositions of the SMAR (5–11°S) basalts are reported in Table 1 along with Sr-Nd-Pb isotope data (Hoernle et al., 2011), with the full elemental data presented in the supplemental materials. The SMAR basalt glasses have δ^{18}O values ranging

from 4.18 to 5.50‰, similar to or slightly lower than that of pristine MORB (5.2 - 5.7‰, Eiler, 2001). The SMAR (5–11°S) basalts show $^{176}Hf/^{177}Hf$ variations ranging from 0.28302 to 0.28338, which are comparable to the $^{176}Hf/^{177}Hf$ variations observed in the Atlantic MORB (0.28302 to 0.28335, Chauvel and Blichert-Toft, 2001). Therein, segment A0 basalts all have high $^{176}Hf/^{177}Hf$ ratios (> 0.2833), and segment A3 basalts have very limited $^{176}Hf/^{177}Hf$ variations that cluster at approximately 0.2831 (Fig. 2). For comparison, segment A1, A2, and A4 basalts display large variations in $^{176}Hf/^{177}Hf$ ratios ranging from 0.2830 to 0.2834 (Fig. 2). Despite their similar ranges, segment A1, A2, and A4 basalts show different trends on the $^{143}Nd/^{144}Nd$ vs. $^{176}Hf/^{177}Hf$ isotope correlation diagram (Fig. 2), which will be further discussed below.

The $\delta^{138/134}Ba$ values range from -0.02 to 0.11‰, with an average $\delta^{138/134}Ba = 0.06 \pm 0.06$‰ (2SD, n=30). Despite the relatively limited Ba isotope variations, there are systematic differences between the basalts from the A0 segment and those from the A1-A4 segments. Student's t-Test showed that the two groups of measurements (A0 and A1-A4) were statistically significant, with a p-value (0.0016) < 0.05. This means that there is a high degree of confidence in the difference between the means of A0 and A1-A4 (also see Fig. 3). In detail, basalts from the A0 segment have $\delta^{138/134}Ba$ values ranging from -0.02 to 0.05‰, whereas basalts from the A1-A4 segments have $\delta^{138/134}Ba$ values ranging from 0.02 to 0.11‰. Despite strong enrichment in incompatible trace elements, the basalts from the A3 seamounts also have very limited Ba isotope variations, with $\delta^{138/134}Ba$ values ranging from 0.04 to 0.07‰.

5. Discussion

5.1. Revised segment-scale Hf-Nd isotope variations and the implications for mantle heterogeneity beneath the SMAR (5–11°S)

The basalts from 5–11°S MAR have a large range of incompatible element abundances and radiogenic isotope ratios, indicating highly heterogeneous magma sources (Paulick et al., 2010; Hoernle et al., 2011; Turner et al., 2015). Different models may explain the chemical heterogeneity of basalts from 5–11°S MAR. As outlined above, the Nd-Pb trends identified in the basalts from 5–11°S MAR may indicate mixing of a common depleted (as represented by segment A0) component and three enriched endmember components (A1, A2, A3+A4, Fig. S1)

(Hoernle et al., 2011). In contrast, the Hf-Nd data of this same area presented by Paulick et al. (2010) suggest two mixing trends. Therein, segments A2 + A3 samples define a trend toward a low $^{176}Hf/^{177}Hf$ depleted endmember while segments A1 + A4 samples define a trend toward a high $^{176}Hf/^{177}Hf$ depleted and both trends extend toward an enriched endmember compositions represented by samples from Ascension Island. Thus, Paulick et al. (2010) argues for a common enriched, Ascension Island-like endmember and two diverging depleted endmembers with different $^{176}Hf/^{177}Hf$ features.

Our new $^{176}Hf/^{177}Hf$ data provide further constraints on the mantle source characteristics of MORB from the SMAR (5–11°S). In the $^{176}Hf/^{177}Hf$-$^{143}Nd/^{144}Nd$ diagram (Fig. 2A), segments A0, A1, A3, and A4 define one coherent trend with a depleted endmember composition represented by samples from segment A0, while the most enriched samples are from segment A3 and the A3 seamounts. For comparison, segment A2 basalts show a large variation in $^{176}Hf/^{177}Hf$ for the given, relatively small $^{143}Nd/^{144}Nd$ range and form a distinctive field below the trend defined by samples from other segments (Fig. 2A). It is notable that our new Hf isotope data from segment A2 exhibit much larger Hf isotope variations and are more dispersed in the Nd-Hf diagram than those presented by Paulick et al. (2010). Moreover, a distinct enriched component is required to explain the observed $^{176}Hf/^{177}Hf$-$^{143}Nd/^{144}Nd$ variations in the A2 basalts (Fig. 2A). The $^{176}Hf/^{177}Hf$-Nd/Hf diagram further suggests that the A1, A2, and A3+A4 basalts likely show three trends with distinctive enriched endmembers (Fig. 2B), which is consistent with that suggested by Hoernle et al. (2011) based on the Nd-Pb diagram. In summary, multiple enriched components are required to explain the geochemical variations along the SMAR (5–11°S), which may reflect different packages of recycled ocean crust and/or metasomatized peridotite (Hoernle et al., 2011; Turner et al., 2015).

It is also notable that the relatively scattered Hf-Nd isotope variations observed in the A2 basalts (Fig. 2A) are hard to simulate with a single mixing line. Multiple Hf-Nd isotope trends have been recognized in global MORB and explained by heterogeneity within the depleted mantle, which might result from the contribution of ancient residual mantle (e.g., Salters et al., 2011; Stracke et al., 2011). Therefore, an additional depleted component, distinct from that sampled by A0 basalts, might exist beneath the A2 segment. However, the most depleted sample from segment A2 has Hf-Nd features close to those from segment A0 (Fig. 2). Thus, the

additional depleted mantle component, if it exists, has little impact on the elemental and isotopic budget of incompatible elements in A2 basalts. Such a depleted component must therefore be volumetrically minor or highly refractory due to prior melt extraction (e.g., Sanfilippo et al, 2019). In other words, the isotope composition of the incompatible elements in the A0 basalts record that of the available depleted component of the ambient upper mantle, which might represent the dominant composition of the depleted endmember of the mid-Atlantic ridge system (e.g., Agranier et al., 2005; Hoernle et al., 2011).

5.2. Barium isotope variations in basalts from the SMAR (5–11°S)

All of the samples investigated here are basaltic (<53 wt.% SiO_2) and no correlation exists between $\delta^{138}Ba$ and indicators of magma differentiation such as MgO (Fig. 4A), arguing against Ba isotope fractionation during fractional crystallization. Barium is highly incompatible ($D_{solid/melt}$ < 0.001, Salters et al., 2002) during mantle melting. Thus, more than 99.99% of the Ba will enter the melt when the melt fraction is > 1%, and no fractionation of Ba isotopes is anticipated to occur during partial melting. The same conclusion applies for fractional crystallization unless mica, amphibole, or alkali feldspar with high Ba content appear as the major crystallization phase (Deng et al., 2021), which is not the case during the fractional crystallization of MORB. Given the highly incompatible behavior of Ba, there is no reason to assume that any detectable Ba isotope fractionation occurs during these processes. The absence of Ba isotope fractionation during modest degrees of fractional crystallization has also been suggested by Ba isotope studies of arc lavas (Nielsen et al., 2020; Wu et al., 2020).

Crustal assimilation may influence the elemental and isotopic compositions of magmas. Oxygen isotope measurements for selected SMAR basalts reveal $\delta^{18}O$ values within the range of or slightly lower than that of pristine MORB (5.2 - 5.7‰, Eiler, 2001) (Fig. 4B). The samples with slightly lower $\delta^{18}O$ values may indicate either a slightly low-$\delta^{18}O$ mantle source or interaction with high-T altered lower oceanic lithosphere (e.g., Bindeman, 2008). Regardless of the reason for the slight oxygen isotope variations, no systematic difference in Ba isotope composition is observed between the low-$\delta^{18}O$ samples and those with pristine mantle-like $\delta^{18}O$ values, thus arguing against the influence of assimilation (Fig. 4B). In addition, there is no correlation between $\delta^{138/134}Ba$ and either Cl/Nb or 1/Ba, as might be expected if Ba isotope compositions were influenced by assimilation of altered oceanic crust or gabbro (Fig. 4C and 4D). The SiO_2 of the

SMAR (5–11°S) basalts also shows no correlation with $^{87}Sr/^{86}Sr$ or Cl/K, further arguing against crustal assimilation (Turner et al., 2015). Accordingly, we infer that the Ba isotope compositions of the SMAR (5–11°S) basalts closely resemble those of their mantle source regions.

Geochemical variations in the SMAR (5–11°S) basalts are likely to reflect mixing between a dominant depleted mantle component sampled by A0 samples and three distinct enriched components that represent different recycled materials to form the A1, A2 and A3+A4 compositions (Hoernle et al., 2011; Turner et al., 2015). The $\delta^{138/134}$Ba ratios of the SMAR (5–11°S) basalts show moderate correlations with Sr-Nd-Pb-Hf isotopes and trace element indicators of enriched components with statistical significance (two-tailed probabilities for the correlation coefficient $P < 0.01$) (Fig. 5). However, no difference in the range of Ba isotope variations is observed among the basalts from within the A1, A2, and A3+A4 segments. Thus, the enriched endmembers involved in the SMAR (5–11°S) basalts have limited Ba isotope variations, very close to that of the ambient depleted mantle source.

5.3. Barium isotope composition of the depleted upper mantle

The Ba isotopic composition of the depleted upper mantle (i.e., the MORB source in the absence of recycled components; e.g., Salters and Stracke, 2004) provide a fundamental baseline for the use of Ba isotopes for tracing crust-mantle interaction. Two methods are applied to estimate the Ba isotope composition of the depleted upper mantle using the current Ba isotope data set of global MORB (67 samples, 26 from this study plus 41 literature data, Fig. 3). One is to use the average $\delta^{138/134}$Ba values of SMAR samples from 4.8°S to 7.6°S (A0 group), which represent the most depleted endmember of the mid-Atlantic ridge system (e.g., Agranier et al., 2005) and are among the most depleted compositions sampled by MORB thus far beneath mid-ocean ridges (e.g., Hofmann, 2014). Using these samples, the endmember composition for DMM is estimated to be $\delta^{138/134}$Ba of 0.03 ± 0.02‰ (2SD/√n, n = 6). An alternative is to consider all those MORB that are highly depleted in incompatible elements. Following Gale et al. (2013), MORB with $(La/Sm)N < 0.8$ are classified as depleted MORB (D-MORB), while those with $(La/Sm)N > 1.5$ are classified as enriched MORB (E-MORB) in this study. Using these criteria, the average $\delta^{138/134}$Ba value of D-MORB (0.05 ± 0.01‰, 2SD/√n, n = 41) might represent the average composition of the depleted upper mantle. Importantly, the results of these two estimates are similar within error but significantly lower than the D-MORB endmember $\delta^{138/134}$Ba value (0.14 ± 0.02‰) suggested by

Nielsen et al. (2018). Accordingly, we suggest that the depleted upper mantle (without recycled components) is characterized by $\delta^{138/134}$Ba values of 0.03 to 0.05‰, and suggest that this value be used as the baseline for future studies on Ba isotopic heterogeneity in the mantle.

5.4. The origin of Ba isotope heterogeneity in MORB

Barium isotope ratios in MORB were observed to correlate with radiogenic isotope and trace element ratios and thus might reflect mixing between a D-MORB endmember, characterized by $\delta^{138/134}$Ba ~0.14‰, and an E-MORB endmember characterized by $\delta^{138/134}$Ba ~0.03‰ (Nielsen et al., 2018). However, the new Ba isotope data presented here show that the SMAR MORB with the most depleted radiogenic isotope compositions (i.e., those from the A0 segment) have a $\delta^{138/134}$Ba ratio of ~0.03‰ (Fig. 6), which is distinctly lower than the value (~0.14‰) estimated by Nielsen et al. (2018). In addition, all but one of the depleted MORB samples with $\delta^{138/134}$Ba values higher than 0.1‰ analyzed by Nielsen et al. (2018) also came from the Mid-Atlantic Ridge. The MORB sampled from segment A0 represent the most depleted compositions sampled thus far from the mid-Atlantic ridge in the perspective of Sr-Nd isotopes (Hoernle et al., 2011; Urann et al., 2020), as well as being among the most depleted basalts from mid-ocean ridges globally (e.g., Hofmann, 2014). Thus, by combining our new SMAR basalt data with published data (Fig. 6), it is clear that the Ba isotope variations in MORB cannot be explained by simple mixing between two distinct endmembers. Instead, Fig. 6 emphasizes that MORB with elevated $^{87}Sr/^{86}Sr$ and low $^{143}Nd/^{144}Nd$ ratios also have variable Ba isotope compositions (-0.04‰ to 0.15‰) compared with the D-MORB endmember defined by the highly depleted MORB from segment A0 of the SMAR. In the following sections, we will discuss the origin of Ba isotope variations in MORB and the mechanisms that might have been responsible for mantle enrichment.

5.4.1 Recycled sediment as the cause of Ba isotope variations in enriched MORB?

The Ba budget of the upper mantle has been considered to be dominated by the recycling of sediments (Nielsen et al. 2018). Previous studies have shown that most marine sediments have a relatively narrow range of Ba isotope compositions (−0.1‰ to 0.1‰) with an average $\delta^{138/134}$Ba of 0.02‰ (±0.05‰, SD, n = 126; data from Bridgestock et al., 2018; Nielsen et al., 2018, 2020). Large Ba isotope variations are observed in material from the upper continental crust (UCC). Therein, granites show extreme $\delta^{138/134}$Ba heterogeneity ranging from positive to negative values (-2‰ to 1‰, Nan et al., 2018; Huang et al., 2021; Deng et al., 2021, 2022). Despite their extreme

heterogeneity, most of the granites with a wide range of $\delta^{138/134}$Ba values are highly fractionated granites, which have much higher SiO_2 contents (> 73 wt.%) and much lower Ba contents (< 150 ppm) than average UCC values (SiO_2 of 66.6 wt.% and Ba of 628 ppm, Rudnick and Gao, 2014). This is also true for the glacial diamictites; those with lower Ba contents (<400 ppm) show greater variation in $\delta^{138/134}$Ba (-0.2 to 0.5‰) than those with higher Ba contents (400 to 1100 ppm, with $\delta^{138/134}$Ba of -0.2 to 0.1‰). For comparison, upper continental crust (UCC) samples that have experienced natural wide-scale sampling processes (i.e., loess and river sediments) have limited Ba isotope variations (−0.05‰ to 0.04‰, Nan et al., 2018). Thus, we regard the weighted average $\delta^{138/134}$Ba of the UCC materials calculated by Nan et al. (2018) (0.00 ± 0.03‰, 2SD/√n, n = 71) as a reasonable estimation of the $\delta^{138/134}$Ba of a putative UCC endmember. Previous studies have also shown the loss of heavy Ba isotopes into the hydrosphere during weathering (Gong et al., 2019, 2020), with the surficial residues becoming enriched in light Ba isotopes. Thus, marine/terrestrial sediments are likely to have Ba isotope compositions equal to or slightly lighter than those inferred for the mantle source of depleted MORB.

Barium isotope fractionation might occur along with fluid/melt release during slab subduction (Gu et al., 2021). Phengite is known to play a dominant role in the large-ion lithophile element budget in subducted sediment and is not completely eliminated from subducted sediment at subarc depths (Hermann and Spandler, 2008; Hermann and Rubatto, 2009). The twelve-fold dodecahedral coordination substitution of Ba in phengite (Rieder et al., 1999) is higher than that in fluid (eightfold coordination, Persson et al., 1995) and silicate melts (~sevenfold coordination, Schlenz et al., 2002). Therefore, fluid/melt is suggested to have isotopically heavier Ba than coexisting phengite in a subduction zone (Xu et al., 2022) and this is supported by Ba isotope studies of metamorphic veins from the Dabie collision orogen (Gu et al., 2021). Conversely, the recycled sediment residue from dehydration/melting in subduction zones might have $\delta^{138/134}$Ba values similar to or lower than that of the precursor sediment. Thus, the recycled sediment materials are likely to have Ba isotope compositions equal to or slightly lighter than those inferred for the mantle source of depleted MORB (0.03 to 0.05‰). Therefore, the Ba isotope variations observed in enriched MORB, especially those that have isotopically heavier Ba ($\delta^{138/134}$Ba up to 0.15‰), cannot be exclusively ascribed to the recycling of sediments.

5.4.2 The role of recycled AOC in the Ba isotope variations observed in enriched MORB

Recycled altered oceanic crust (AOC) may play an important role in mantle enrichment (e.g., Allègre and Turcotte, 1986; Eiler et al., 2000). A large variation in $\delta^{138/134}$Ba ranging from −0.11‰ to 0.40‰ is observed in AOC (Nielsen et al., 2018), which is likely caused by complex interaction with seawater-derived fluids. Global seawater has $\delta^{138/134}$Ba ranging from 0.3 to 0.6‰ (Horner et al., 2015; Cao et al., 2016; Hsieh and Henderson, 2017; Bates et al., 2017; Bridgestock et al., 2018; Crockford et al., 2019). Thus, if isotopic exchange of Ba with seawater occurs within AOC without significant loss or gain of Ba, as indicated by the study of the composite AOC samples (Kelley et al., 2003), this might lead to the elevation of $\delta^{138/134}$Ba in the AOC (Nielsen et al., 2018). This interpretation is also supported by the low $\delta^{138/134}$Ba values observed in the endmember vent fluid from MOR hydrothermal systems (-0.17 to 0.09‰, Hsieh et al., 2021), which likely represents the primary outflux of fluid produced by the interaction between seawater and oceanic crust. On the other hand, previous studies also demonstrate that light Ba isotopes are preferentially incorporated/adsorbed on secondary minerals including barite, clays and Fe-Mn (oxyhydr)oxides during alteration (e.g., Bridgestock et al., 2018; Gong et al., 2020). In summary, the Ba isotope composition of AOC could be both heavier or lighter than that of fresh MORB, and the Ba isotope variations in the enriched MORB might be explained by the recycling of AOC.

To explore the effects of recycling of oceanic crust on the Ba isotope compositions of MORB, melting and mixing between recycled oceanic crust and depleted mantle were modeled. As recorded in Table 2, the trace element and Sr-Nd isotope compositions of the average depleted MORB mantle (A-DMM) endmembers from Workman and Hart (2005) were used in the modeling. We investigated both recycled AOC (Staudigel et al., 1996) and an assumed bulk recycled oceanic crust (ROC, Stracke et al., 2003) as endmembers in the melting and mixing models to test how the addition of these materials might produce Ba isotope and geochemical heterogeneity in the mantle (Table 2). The Sr-Nd isotope composition of the recycled AOC/ROC was calculated using a single-stage evolution model (Stracke et al., 2003) assuming a recycling age of 1 Ga since the residence time of the enriched reservoir is thought to be 0.3 to 1.5 Ga (Allègre et al., 1996; Rehkämper and Hofmann, 1997; Donnelly et al., 2004). The $\delta^{138/134}$Ba of the DMM endmember was chosen to be 0.03‰ based on the Ba isotope composition of the depleted MORB from the A0 segment of the SMAR (5-11°S). The $\delta^{138/134}$Ba of recycled AOC was chosen as 0.25‰ based on published AOC data (Nan et al., 2017; Nielsen et al., 2018) and to fit the observed Ba isotope variations in MORB. The $\delta^{138/134}$Ba of the bulk ROC was calculated by mixing 25% AOC + 25% N-MORB + 50%

gabbro (Stracke et al., 2003), with the $\delta^{138/134}$Ba of AOC, N-MORB, and gabbro chosen to be 0.25‰, 0.03‰, and 0.03‰, respectively (Table 2). The trace element composition of DMM melts was calculated for modal melting of spinel peridotite with a total melting extent (F) of 10%, while the composition of the melt derived from the composite recycled materials was calculated assuming modal melting of pyroxenite (cf. Turner et al., 2015) with F = 10% (Fig. 6 and Fig. 7). Partition coefficients ($D_{solid\text{-}melt}$) for both peridotite and MORB-like pyroxenite (eclogite) were taken from Stracke and Bourdon (2009). For simplicity, we assumed that no reaction occurs between the pyroxenite melts and the ambient peridotite before melt mixing, as suggested by previous work (e.g., Hirschmann and Stolper, 1996; Stracke and Bourdon, 2009; Yang et al., 2020). Variable recycling age of the recycled components (0.3 to 2.0 Ga, Fig. S2) and degrees of partial melting (1 to 20%, Fig. S3) were also explored to assess how these variations influence the modeled mixing trend.

As shown in Fig. 6 and Fig. 7, the calculated trends for mixtures of melts from DMM and AOC display rapid increases in $\delta^{138/134}$Ba with relatively little modification of Sr-Nd isotopes and La/Sm ratios, which could explain why the majority of the MORB samples have high $\delta^{138/134}$Ba. Thus, our models suggest that the AOC provides a considerable explanation for the Ba budget of the mantle source of enriched MORB. Nevertheless, it is difficult to reconcile all of the observed trace element ratios and Ba isotope variations by mixing between depleted peridotite melts from DMM and pyroxenite melts from recycled oceanic crust, even when variable Ba isotope compositions of the recycled AOC/ROC endmember (now shown), variable age of the recycled components (Fig. S2) and variable degrees of partial melting (Fig. S3) are considered. In addition, many of the enriched MORB samples have elevated Rb/Sr, Ba/La, and Th/La and low Zr/Pb, Ce/Pb, Nb/Th ratios, which cannot be explained by mixing between DMM and AOC/ROC melts. This is because the supposed recycled oceanic crust components only show moderate enrichment of Rb, Ba, and Th compared to Sr and La, and have higher rather than lower Zr/Pb, Ce/Pb, Nb/Th ratios compared to that of DMM. For comparison, marine/terrestrial sediments show much higher Rb/Sr, Ba/La, and Th/La ratios and lower Zr/Pb, Ce/Pb, and Nb/Th ratios than those of recycled oceanic crust and DMM. Thus, to explain the geochemical features of these MORB samples, a contribution from sediments in addition to the recycled oceanic crust to their source region is required.

5.4.3 Recycling of multiple crustal components into the convecting upper mantle

To further explore the effects of crustal recycling on the Ba isotope composition of MORB, we now consider the addition of a composite component containing variable proportions of AOC and sediment. The chemical and Sr-Nd isotopic compositions of GLOSS (Fig. 6) (Plank, 2014) and average UCC (Fig. S3) (Goldstein and Jacobsen, 1988; Chauvel et al. 2014; Rudnick and Gao, 2014) are used to represent the subducted marine and terrestrial sediments, respectively (Table 2). The $\delta^{138/134}$Ba values of the GLOSS and UCC endmembers are relatively well constrained by previous studies to be 0.02‰ and 0.00‰ respectively, and are used for the multicomponent models. The $\delta^{138/134}$Ba of the AOC endmember was chosen to be 0.25‰ to calculate the mixture of composite recycled materials. Considering the minor amounts of sediment in the composite recycled component (< 6% in the models), the lithologies of the recycled component are dominated by the recycled oceanic crust. We used the pyroxenite melting model for these simulations, with $D_{solid\text{-}melt}$ being the same as used for modeling the AOC-DMM mixture (Stracke and Bourdon 2009).

The results indicate that the overall variations in a variety of trace element ratios (i.e., Th/La, Zr/Pb, Rb/Sr and Ba/La), radiogenic Sr-Nd isotopes and Ba stable isotopes can be explained by mixing between pyroxenite melts derived from AOC (+ SED) and depleted peridotite melts (Fig. 6 and Fig. S3). Increasing the contribution from sediment to the composite recycled component leads to more variable Sr-Nd isotope and trace element ratios in the mixtures (e.g., Zr/Pb, Ba/La and Th/La) combined with a limited range in Ba isotopes, which are consistent with that observed in enriched MORB. Our models indicate that the mixing of up to ~10 to 30% AOC pyroxenite melts, with or without the involvement of a small amount of sediment, can simulate most of the observed variation in Sr-Nd-Ba isotopes and key trace element ratios in MORB. The overall consistency of the models was further verified by the relations between some key radiogenic isotopes (Sr and Nd isotopes) and trace element ratios (Ba/La, Nb/Th, and Zr/Pb ratios) (Fig. S4). This result is also consistent with a recent study that suggested that 10 to 30% admixing of pyroxenite melts with D-MORB-like melts is required to explain the ~14% lower Ge/Si ratios in E-MORB compared with D-MORB (Yang et al., 2020).

The magnitude of the $(La/Sm)_N$ enrichment in the enriched MORB is difficult to reproduce by mixing between melts of depleted mantle and recycled AOC (+ SED) unless the melt fraction is extremely low (F < 2%) (Fig. 7). The extent of peridotite melting to produce MORB is constrained

to lie between 5% and 20% (e.g., Klein and Langmuir, 1987; Hofmann, 1988). Experimental studies have shown that the pyroxenite solidus could be >200°C lower than that of peridotite (e.g., Pertermann and Hirschmann, 2003; Kogiso et al., 2004). Therefore, the extent of pyroxenite melting within the region beneath the ridges is likely to be similar to or higher than that of peridotite (e.g., Dasgupta et al., 2004; Sobolev et al., 2007). Therefore, pyroxenite is unlikely to generate ultralow-degree melts ($F < \sim 2\%$) beneath ridges. The mixing between melts from recycled materials with a high proportion (>15%) of GLOSS ($(La/Sm)_N$ = 3.1, Plank, 2014) or UCC ($(La/Sm)_N$ = 4.3, Rudnick and Gao, 2014) and D-MORB could potentially explain the high $(La/Sm)_N$ in enriched MORB. However, to simulate the high $(La/Sm)_N$ (> 2.5) of the enriched MORB, the added recycled component will drive the Nb/Th (< 2.5), Ce/Pb (< 6), and Zr/Pb (< 25) much lower than that observed (Fig. 6).

Recycled oceanic lithospheric mantle that has been metasomatized by small volumes of incompatible element-rich ultralow-degree melts (F < 1%) in the mantle wedge beneath arcs (Donnelly et al., 2004) or in the thickening oceanic lithosphere (e.g., Niu et al., 2002) has been advocated as the main way to entrain the enriched component into the source of MORB. The fractionated ratios of highly incompatible elements, such as the high $(La/Sm)_N$ ratios observed in highly enriched MORB, can be explained by this scenario. However, melting models suggest that the Zr/Pb ratios observed in MORB cannot be exclusively ascribed to recycled metasomatized mantle lithosphere. This is because ultralow-degree melts (F < 1%), even from dehydrated AOC (initial Zr/Pb ratio of ~710), have low Zr/Pb ratios (<200) that do not account for the variable Zr/Pb ratios in MORB (Fig. 8). On the other hand, the mixing of melts from DMM and AOC (+SED) successfully simulates the variable Zr/Pb ratios (Fig. 8) as well as the Ba isotope variations (Fig. 6). The metasomatized peridotite model also fails to explain the low Ge/Si ratios observed in many enriched MORB (Yang et al., 2020). Thus, although recycled lithospheric mantle that has been metasomatized by ultralow-degree melts (F < 1%) may be an important component for some enriched MORB (especially those that have highly fractionated incompatible element ratios), it seems unlikely to be able to provide a universal explanation for enriched MORB. Our presented models suggest that both recycled altered oceanic crust and sediments are needed on regional and global scales to explain the observed stable Ba and radiogenic isotope and trace element variations. While further work is required to better understand the nature, diversity, and melting process in

the mantle source of MORB, our study shows that the sub-ridge mantle is a diverse agglomerate of various recycled components and residual mantle.

6. Conclusions

We present Ba isotope data for MORB from the SMAR (5–11°S). Combined with published MORB data, our study leads to the following conclusions:

(1) SMAR basalts have $\delta^{138/134}$Ba ratios that range from −0.02‰ to 0.11‰ and vary systematically with indices of mantle enrichment that reflect the involvement of recycled components. However, no Ba isotope difference is observed in the four MORB segments (A1 to A4) between the Ascension and Bode Verde Fracture Zones, even though they form different arrays in Pb-Nd isotope space that have been ascribed to contributions from three different enriched end-member components (Hoernle et al., 2011). Thus, these enriched components appear to have indistinguishable Ba isotope signatures.

(2) Combining our new measurements with literature data, this study shows that the depleted upper mantle is likely to be characterized by $\delta^{138/134}$Ba values of 0.03 to 0.05‰, which are significantly lower than those suggested by Nielsen et al. (2018) ($\delta^{138/134}$Ba ~0.14‰). This refined baseline value should help further facilitate the application of Ba isotopes to trace the mass transfer between surficial and deep-seated reservoirs.

(3) No single global correlation between Ba isotopes and other geochemical or tectonic parameters were observed. Modeling of melting and mixing between recycled materials and depleted mantle indicates that the variable Ba isotope compositions of enriched MORB (-0.04‰ to 0.15‰) require contributions from a range of recycled materials. Therefore, both recycled AOC and sediments play important roles in the chemical budget of the convecting upper mantle, especially for incompatible elements such as Ba.

Acknowledgment

We would like to thank Andreas Stracke, Matthew Jackson, and an anonymous reviewer for constructive review comments that led to improvements in the manuscript. Major contributions

were made by Peter Wieland, Yi-Jen Lai, and John Creech for technical and analytical support in the Macquarie University (Australia) GeoAnalytical (MQGA) laboratories. We thank Thermo Scientific and the Macquarie University Deputy Vice-Chancellor of Research for equipment support and postdoctoral salaries in the Macquarie University–Thermo Fisher Isotope Development laboratories. This study was supported by funds from the National Natural Science Foundation of China (42173018).

Appendix. Supplementary Materials

Supplementary figures

Supplementary data

References

Agranier, A., Blichert-Toft, J., Graham, D., Debaille, V., Schiano, P. and Albarède, F. (2005) The spectra of isotopic heterogeneities along the mid-Atlantic Ridge. Earth and Planetary Science Letters 238, 96-109.

Allègre, C.J., Hamelin, B., Provost, A. and Dupré, B. (1987) Topology in isotopic multispace and origin of mantle chemical heterogeneities. Earth and Planetary Science Letters 81, 319-337.

Allègre, C.J., Moreira, M. and Staudacher, T.J.G.R.L. (1995) 4He/^{3}He dispersion and mantle convection. 22, 2325-2328.

Allègre, C.J. and Turcotte, D.L. (1986) Implications of a two-component marble-cake mantle. Nature 323, 123-127.

Almeev, R., Holtz, F., Koepke, J., Haase, K. and Devey, C. (2007) Depths of Partial Crystallization of H2O-bearing MORB: Phase Equilibria Simulations of Basalts at the MAR near Ascension Island (7–11°S). Journal of Petrology 49, 25-45.

An, Y.J., Li, X. and Zhang, Z.F. (2020) Barium Isotopic Compositions in Thirty-Four Geological Reference Materials Analysed by MC-ICP-MS. Geostandards and Geoanalytical Research 44, 183-199.

Arevalo, R. and McDonough, W.F. (2010) Chemical variations and regional diversity observed in MORB. Chemical Geology 271, 70-85.

Bai, R., Jackson, M.G., Huang, F., Moynier, F., Devos, G., Halldórsson, S.A., Lisiecki, L., Yin, H., Peng, Y. and Nan, X. (2022) Barium isotopes in ocean island basalts as tracers of mantle processes. Geochimica et Cosmochimica Acta.

Bates, S.L., Hendry, K.R., Pryer, H.V., Kinsley, C.W., Pyle, K.M., Woodward, E.M.S. and Horner, T.J. (2017) Barium isotopes reveal role of ocean circulation on barium cycling in the Atlantic. Geochimica et Cosmochimica Acta 204, 286-299.

Bebout, G.E. (2014) 4.20 - Chemical and Isotopic Cycling in Subduction Zones, in: Holland, H.D., Turekian, K.K. (Eds.), Treatise on Geochemistry (Second Edition). Elsevier, Oxford, pp. 703-747.

Bindeman, I. (2008) Oxygen Isotopes in Mantle and Crustal Magmas as Revealed by Single Crystal Analysis. Reviews in Mineralogy and Geochemistry 69, 445-478.

Blichert-Toft, J. and Albarède, F. (1997) The Lu-Hf isotope geochemistry of chondrites and the evolution of the mantle-crust system. Earth and Planetary Science Letters 148, 243-258.

Bridgestock, L., Hsieh, Y.-T., Porcelli, D., Homoky, W.B., Bryan, A. and Henderson, G.M. (2018) Controls on the barium isotope compositions of marine sediments. Earth and Planetary Science Letters 481, 101-110.

Brozena, J.M. (1986) Temporal and spatial variability of seafloor spreading processes in the northern south Atlantic. 91, 497-510.

Bruguier, N.J., Minshull, T.A. and Brozena, J.M. (2003) Morphology and tectonics of the Mid-Atlantic Ridge, 7°–12°S. 108.

Cao, Z., Siebert, C., Hathorne, E.C., Dai, M. and Frank, M. (2016) Constraining the oceanic barium cycle with stable barium isotopes. Earth and Planetary Science Letters 434, 1-9.

Chauvel, C. and Blichert-Toft, J. (2001) A hafnium isotope and trace element perspective on melting of the depleted mantle. Earth and Planetary Science Letters 190, 137-151.

Chauvel, C., Garçon, M., Bureau, S., Besnault, A., Jahn, B.-m. and Ding, Z. (2014) Constraints from loess on the Hf–Nd isotopic composition of the upper continental crust. Earth and Planetary Science Letters 388, 48-58.

Crockford, P.W., Wing, B.A., Paytan, A., Hodgskiss, M.S.W., Mayfield, K.K., Hayles, J.A., Middleton, J.E., Ahm, A.-S.C., Johnston, D.T., Caxito, F., Uhlein, G., Halverson, G.P., Eickmann, B., Torres, M. and Horner, T.J. (2019) Barium-isotopic constraints on the origin of post-Marinoan barites. Earth and Planetary Science Letters 519, 234-244.

Dasgupta, R., Hirschmann, M.M. and Withers, A.C. (2004) Deep global cycling of carbon constrained by the solidus of anhydrous, carbonated eclogite under upper mantle conditions. Earth and Planetary Science Letters 227, 73-85.

DeMets, C., Gordon, R.G., Argus, D.F. and Stein, S. (1994) Effect of recent revisions to the geomagnetic reversal time scale on estimates of current plate motions. 21, 2191-2194.

Deng, G., Jiang, D., Zhang, R., Huang, J., Zhang, X. and Huang, F. (2022) Barium isotopes reveal the role of deep magmatic fluids in magmatic-hydrothermal evolution and tin enrichment in granites. Earth and Planetary Science Letters 594, 117724.

Deng, G., Kang, J., Nan, X., Li, Y., Guo, J., Ding, X. and Huang, F. (2021) Barium isotope evidence for crystal-melt separation in granitic magma reservoirs. Geochimica et Cosmochimica Acta 292, 115-129.

Donnelly, K.E., Goldstein, S.L., Langmuir, C.H. and Spiegelman, M. (2004) Origin of enriched ocean ridge basalts and implications for mantle dynamics. Earth and Planetary Science Letters 226, 347-366.

Eiler, J.M. (2001) Oxygen isotope variations of basaltic lavas and upper mantle rocks. Reviews in Mineralogy and geochemistry 43, 319-364.

Eiler, J.M., Schiano, P., Kitchen, N. and Stolper, E.M. (2000) Oxygen-isotope evidence for recycled crust in the sources of mid-ocean-ridge basalts. Nature 403, 530-534.

Gale, A., Dalton, C.A., Langmuir, C.H., Su, Y. and Schilling, J.G. (2013) The mean composition of ocean ridge basalts. Geochemistry, Geophysics, Geosystems 14, 489-518.

Geldmacher, J., Hoernle, K., Klügel, A., Bogaard, P.v.d., Wombacher, F. and Berning, B. (2006) Origin and geochemical evolution of the Madeira-Tore Rise (eastern North Atlantic). 111.

Goldstein, S.J. and Jacobsen, S.B. (1988) Nd and Sr isotopic systematics of river water suspended material: implications for crustal evolution. Earth and Planetary Science Letters 87, 249-265.

Gong, Y., Zeng, Z., Cheng, W., Lu, Y., Zhang, L., Yu, H. and Huang, F. (2020) Barium isotopic fractionation during strong weathering of basalt in a tropical climate. Environment International 143, 105896.

Gong, Y., Zeng, Z., Zhou, C., Nan, X., Yu, H., Lu, Y., Li, W., Gou, W., Cheng, W. and Huang, F. (2019) Barium isotopic fractionation in latosol developed from strongly weathered basalt. Science of The Total Environment 687, 1295-1304.

Gou, L.-F., Jin, Z., Galy, A., Gong, Y.-Z., Nan, X.-Y., Jin, C., Wang, X.-D., Bouchez, J., Cai, H.-M. and Chen, J.-B. (2020) Seasonal riverine barium isotopic variation in the middle Yellow River: Sources and fractionation. Earth and Planetary Science Letters 531, 115990.

Gu, X.-F., Guo, S., Yu, H.-M., Xu, J. and Huang, F. (2021) Behavior of barium isotopes during high-pressure metamorphism and fluid evolution. Earth and Planetary Science Letters 575, 117176.

Hao, L.-L., Nan, X.-Y., Kerr, A.C., Li, S.-Q., Wu, Y.-B., Wang, H. and Huang, F. (2022) Mg-Ba-Sr-Nd isotopic evidence for a mélange origin of early Paleozoic arc magmatism. Earth and Planetary Science Letters 577, 117263.

Hermann, J. and Rubatto, D. (2009) Accessory phase control on the trace element signature of sediment melts in subduction zones. Chemical Geology 265, 512-526.

Hermann, J. and Spandler, C.J. (2008) Sediment Melts at Sub-arc Depths: an Experimental Study. Journal of Petrology 49, 717-740.

Hirschmann, M.M. and Stolper, E.M. (1996) A possible role for garnet pyroxenite in the origin of the "garnet signature" in MORB. Contributions to Mineralogy and Petrology 124, 185-208.

Hoernle, K., Hauff, F., Kokfelt, T.F., Haase, K., Garbe-Schönberg, D. and Werner, R. (2011) On- and off-axis chemical heterogeneities along the South Atlantic Mid-Ocean-Ridge (5–11°S): Shallow or deep recycling of ocean crust and/or intraplate volcanism? Earth and Planetary Science Letters 306, 86-97.

Hofmann, A.W. (1988) Chemical differentiation of the Earth: the relationship between mantle, continental crust, and oceanic crust. Earth and Planetary Science Letters 90, 297-314.

Hofmann, A.W. (2007) 2.03 - Sampling Mantle Heterogeneity through Oceanic Basalts: Isotopes and Trace Elements, in: Holland, H.D., Turekian, K.K. (Eds.), Treatise on Geochemistry. Pergamon, Oxford, pp. 1-44.

Horner, T.J., Kinsley, C.W. and Nielsen, S.G. (2015) Barium-isotopic fractionation in seawater mediated by barite cycling and oceanic circulation. Earth and Planetary Science Letters 430, 511-522.

Hsieh, Y.-T., Bridgestock, L., Scheuermann, P.P., Seyfried, W.E. and Henderson, G.M. (2021) Barium isotopes in mid-ocean ridge hydrothermal vent fluids: A source of isotopically heavy Ba to the ocean. Geochimica et Cosmochimica Acta 292, 348-363.

Hsieh, Y.-T. and Henderson, G.M. (2017) Barium stable isotopes in the global ocean: Tracer of Ba inputs and utilization. Earth and Planetary Science Letters 473, 269-278.

Huang, F., Bai, R., Deng, G., Liu, X. and Li, X. (2021) Barium isotope evidence for the role of magmatic fluids in the origin of Himalayan leucogranites. Science Bulletin.

Jackson, M.G. and Dasgupta, R. (2008) Compositions of HIMU, EM1, and EM2 from global trends between radiogenic isotopes and major elements in ocean island basalts. Earth and Planetary Science Letters 276, 175-186.

Jenner, F.E. and O'Neill, H.S.C. (2012) Analysis of 60 elements in 616 ocean floor basaltic glasses. Geochemistry, Geophysics, Geosystems 13, Q02005.

Kelley, K.A., Plank, T., Ludden, J. and Staudigel, H. (2003) Composition of altered oceanic crust at ODP Sites 801 and 1149. 4.

Kessel, R., Schmidt, M.W., Ulmer, P. and Pettke, T. (2005) Trace element signature of subduction-zone fluids, melts and supercritical liquids at 120-180 km depth. Nature 437, 724-727.

Klein, E.M. and Langmuir, C.H. (1987) Global correlations of ocean ridge basalt chemistry with axial depth and crustal thickness. Journal of Geophysical Research: Solid Earth 92, 8089-8115.

KOGISO, T., HIRSCHMANN, M.M. and PERTERMANN, M. (2004) High-pressure Partial Melting of Mafic Lithologies in the Mantle. Journal of Petrology 45, 2407-2422.

Kogiso, T., Tatsumi, Y. and Nakano, S. (1997) Trace element transport during dehydration processes in the subducted oceanic crust: 1. Experiments and implications for the origin of ocean island basalts. Earth and Planetary Science Letters 148, 193-205.

Li, W.-Y., Yu, H.-M., Xu, J., Halama, R., Bell, K., Nan, X.-Y. and Huang, F. (2019) Barium isotopic composition of the mantle: Constraints from carbonatites. Geochimica et Cosmochimica Acta.

Minshull, T.A., Bruguier, N.J. and Brozena, J.M. (1998) Ridge-plume interactions or mantle heterogeneity near Ascension Island? Geology 26, 115-118.

Möller, H. (2002) Magma genesis and mantle sources at the Mid-Atlantic Ridge East of Ascension Island.

Nan, X.-Y., Yu, H.-M., Rudnick, R.L., Gaschnig, R.M., Xu, J., Li, W.-Y., Zhang, Q., Jin, Z.-D., Li, X.-H. and Huang, F. (2018) Barium isotopic composition of the upper continental crust. Geochimica et Cosmochimica Acta 233, 33-49.

Nan, X., Yu, H. and Gao, Y. (2017) Barium isotope composition of altered oceanic crust from the IODP Site 1256 at the East Pacific Rise, AGU Fall Meeting Abstracts, pp. V33C-0534.

Nielsen, S.G., Horner, T.J., Pryer, H.V., Blusztajn, J., Shu, Y., Kurz, M.D. and Le Roux, V. (2018) Barium isotope evidence for pervasive sediment recycling in the upper mantle. Science Advances 4.

Nielsen, S.G., Shu, Y., Auro, M., Yogodzinski, G., Shinjo, R., Plank, T., Kay, S.M. and Horner, T.J. (2020) Barium isotope systematics of subduction zones. Geochimica et Cosmochimica Acta 275, 1-18.

Niu, Y., Regelous, M., Wendt, I.J., Batiza, R. and O'Hara, M.J. (2002) Geochemistry of near-EPR seamounts: importance of source vs. process and the origin of enriched mantle component. Earth and Planetary Science Letters 199, 327-345.

Paulick, H., Münker, C. and Schuth, S. (2010) The influence of small-scale mantle heterogeneities on Mid-Ocean Ridge volcanism: Evidence from the southern Mid-Atlantic Ridge (7°30′S to 11°30′S) and Ascension Island. Earth and Planetary Science Letters 296, 299-310.

Persson, I., Sandström, M. and Yokoyama, H. (1995) Structure of the Solvated Strontium and Barium Ions in Aqueous, Dimethyl Sulfoxide and Pyridine Solution, and Crystal

Structure of Strontium and Barium Hydroxide Octahydrate %J Zeitschrift für Naturforschung A. 50, 21-37.

PERTERMANN, M. and HIRSCHMANN, M.M. (2003) Anhydrous Partial Melting Experiments on MORB-like Eclogite: Phase Relations, Phase Compositions and Mineral–Melt Partitioning of Major Elements at 2–3 GPa. Journal of Petrology 44, 2173-2201.

Plank, T. (2014) 4.17 - The Chemical Composition of Subducting Sediments, in: Holland, H.D., Turekian, K.K. (Eds.), Treatise on Geochemistry (Second Edition). Elsevier, Oxford, pp. 607-629.

Plank, T. and Langmuir, C.H. (1998) The chemical composition of subducting sediment and its consequences for the crust and mantle. Chemical Geology 145, 325-394.

Pretet, C., Zuilen, K., Nägler, T.F., Reynaud, S., Böttcher, M.E. and Samankassou, E. (2016) Constraints on barium isotope fractionation during aragonite precipitation by corals. The Depositional Record.

Rampone, E. and Hofmann, A.W. (2012) A global overview of isotopic heterogeneities in the oceanic mantle. Lithos 148, 247-261.

Rehka¨mper, M. and Hofmann, A.W. (1997) Recycled ocean crust and sediment in Indian Ocean MORB. Earth and Planetary Science Letters 147, 93-106.

Rieder, M., Cavazzini, G., D'yakonov, Y.S., Frank-Kamenetskii, V.A., Gottardi, G., Guggenheim, S., Koval', P.V., Müller, G., Neiva, A.M.R., Radoslovich, E.W., Robert, J.L., Sassi, F.P., Takeda, H., Weiss, Z. and Wones, D.R. (1999) Nomenclature of the micas. Mineralogical Magazine 63, 267-279.

Rudnick, R.L. and Gao, S. (2014) 4.1 - Composition of the Continental Crust, in: Holland, H.D., Turekian, K.K. (Eds.), Treatise on Geochemistry (Second Edition). Elsevier, Oxford, pp. 1-51.

Ryan, W.B.F., Carbotte, S.M., Coplan, J.O., O'Hara, S., Melkonian, A., Arko, R., Weissel, R.A., Ferrini, V., Goodwillie, A., Nitsche, F., Bonczkowski, J. and Zemsky, R. (2009) Global Multi-Resolution Topography synthesis. 10.

Salters, V.J., Longhi, J.E. and Bizimis, M.J.G., Geophysics, Geosystems (2002) Near mantle solidus trace element partitioning at pressures up to 3.4 GPa. 3, 1-23.

Salters, V.J. and Stracke, A. (2004) Composition of the depleted mantle. Geochemistry, Geophysics, Geosystems 5.

Salters, V.J.M., Mallick, S., Hart, S.R., Langmuir, C.E. and Stracke, A. (2011) Domains of depleted mantle: New evidence from hafnium and neodymium isotopes. Geochemistry, Geophysics, Geosystems 12.

Sanfilippo, A., Salters, V., Tribuzio, R. and Zanetti, A. (2019) Role of ancient, ultra-depleted mantle in Mid-Ocean-Ridge magmatism. Earth and Planetary Science Letters 511, 89-98.

Schlenz, H., Kirfel, A., Schulmeister, K., Wartner, N., Mader, W., Raberg, W., Wandelt, K., Oligschleger, C., Bender, S., Franke, R., Hormes, J., Hoffbauer, W., Lansmann, V., Jansen, M., Zotov, N., Marian, C., Putz, H. and Neuefeind, J. (2002) Structure analyses of Ba-silicate glasses. Journal of Non-Crystalline Solids 297, 37-54.

Sobolev, A.V., Hofmann, A.W., Kuzmin, D.V., Yaxley, G.M., Arndt, N.T., Chung, S.-L., Danyushevsky, L.V., Elliott, T., Frey, F.A., Garcia, M.O., Gurenko, A.A., Kamenetsky, V.S., Kerr, A.C., Krivolutskaya, N.A., Matvienkov, V.V., Nikogosian, I.K., Rocholl, A., Sigurdsson, I.A., Sushchevskaya, N.M. and Teklay, M. (2007) The Amount of Recycled Crust in Sources of Mantle-Derived Melts. Science 316, 412-417.

Staudigel, H., Plank, T., White, B. and Schmincke, H.-U. (1996) Geochemical Fluxes During Seafloor Alteration of the Basaltic Upper Oceanic Crust: DSDP Sites 417 and 418, Subduction, pp. 19-38.

Stracke, A. (2012) Earth's heterogeneous mantle: A product of convection-driven interaction between crust and mantle. Chemical Geology 330-331, 274-299.

Stracke, A., Bizimis, M. and Salters, V.J.M. (2003) Recycling oceanic crust: Quantitative constraints. Geochemistry, Geophysics, Geosystems 4.

Stracke, A. and Bourdon, B. (2009) The importance of melt extraction for tracing mantle heterogeneity. Geochimica et Cosmochimica Acta 73, 218-238.

Stracke, A., Snow, J.E., Hellebrand, E., von der Handt, A., Bourdon, B., Birbaum, K. and Günther, D. (2011) Abyssal peridotite Hf isotopes identify extreme mantle depletion. Earth and Planetary Science Letters 308, 359-368.

Sun, S.-S. and McDonough, W.F. (1989) Chemical and isotopic systematics of oceanic basalts: implication for mantle composition and processes. In Saunders A. D., Norry M.J., eds. Magmatism in the Ocean Basins 42, 313-345.

Turner, S., Kokfelt, T., Hauff, F., Haase, K., Lundstrom, C., Hoernle, K., Yeo, I. and Devey, C. (2015) Mid-ocean ridge basalt generation along the slow-spreading, South Mid-Atlantic Ridge (5–11°S): Inferences from 238U–230Th–226Ra disequilibria. Geochimica et Cosmochimica Acta 169, 152-166.

Urann, B.M., Dick, H.J.B., Parnell-Turner, R. and Casey, J.F. (2020) Recycled arc mantle recovered from the Mid-Atlantic Ridge. Nature Communications 11, 3887.

Valley, J.W., Kitchen, N., Kohn, M.J., Niendorf, C.R. and Spicuzza, M.J. (1995) UWG-2, a garnet standard for oxygen isotope ratios: Strategies for high precision and accuracy with laser heating. Geochimica et Cosmochimica Acta 59, 5223-5231.

Wei, W., Zeng, Z., Shen, J., Tian, L.-L., Wei, G.-Y., Ling, H.-F. and Huang, F. (2021) Dramatic changes in the carbonate-hosted barium isotopic compositions in the Ediacaran Yangtze Platform. Geochimica et Cosmochimica Acta 299, 113-129.

White, W.M.J.G.P. (2015) Probing the Earth's deep interior through geochemistry. 4.

Workman, R.K. and Hart, S.R. (2005) Major and trace element composition of the depleted MORB mantle (DMM). Earth and Planetary Science Letters 231, 53-72.

Wu, F., Turner, S. and Schaefer, B.F. (2020) Mélange versus fluid and melt enrichment of subarc mantle: A novel test using barium isotopes in the Tonga-Kermadec arc. Geology.

Xiaoyun, N., Huimin, Y., Jinting, K. and Fang, H. (2022) Re-visiting barium isotope compositions of mid-ocean ridge basalts and the implications. JUSTC 52, 1-1-1-8.

Xu, Z., Zheng, Y.-F. and Zhao, Z.-F. (2022) Barium isotope fractionation during dehydration melting of the subducting oceanic crust: Geochemical evidence from OIB-like continental basalts. Chemical Geology, 120751.

Yang, S., Humayun, M. and Salters, V.J.M. (2020) Elemental constraints on the amount of recycled crust in the generation of mid-oceanic ridge basalts (MORBs). Science Advances 6, eaba2923.

Yi, D., Zhao, J., Li, C. and Peng, X. (2022) Crustal Contaminations Responsible for the Petrogenesis of Basalts from the Emeishan Large Igneous Province, NW China: New Evidence from Ba Isotopes. Journal of Earth Science 33, 109-120.

Yu, H.-M., Nan, X.-Y., Wu, F., Widom, E., Li, W.-Y., Kuentz, D. and Huang, F.J.C.G. (2022) Barium isotope evidence of a fluid-metasomatized mantle component in the source of Azores OIB. 610, 121097.

Zack, T., Rivers, T., Foley, S.J.C.t.M. and Petrology (2001) Cs–Rb–Ba systematics in phengite and amphibole: an assessment of fluid mobility at 2.0 GPa in eclogites from Trescolmen, Central Alps. 140, 651-669.

Zhang, F., Frýda, J., Fakhraee, M., Lin, Y.-b., Wei, G.-Y., Cao, M., Li, N., Zhou, J., Frýdová, B., Wei, H. and Shen, S.-z. (2022) Marine anoxia as a trigger for the largest Phanerozoic positive carbon isotope excursion: Evidence from carbonate barium isotope record. Earth and Planetary Science Letters 584, 117421.

Zhao, Y.-P., Tang, Y.-J., Xu, J., Zeng, Z., Ying, J.-F., Tian, H.-C. and Huang, F. (2021) Barium isotope evidence for recycled crustal materials in the mantle source of continental basalts. Lithos, 106111.

Zindler, A., Hart, S.J.A.r.o.e. and sciences, p. (1986) Chemical geodynamics. 14, 493-571.

Table 1

Sr-Nd-Pb-Hf-O-Ba isotope data for SMAR (5-11°S) basalts

Sample	Segment	Lat. ˚S	Long. ˚W	$^{87}Sr/^{86}Sr$	$^{143}Nd/^{144}Nd$	$^{208}Pb/^{206}Pb$	$^{177}Hf/^{176}Hf$	2s.e.	$\delta^{18}O$	$\delta^{138/134}Ba$	2SD	N(i)
118VSR	4.8 S	4.804	12.371	0.702114	0.513311	2.1080				-0.02	0.04	6(1)
119VSR	4.8 S	4.804	12.358	0.702114	0.513305	2.1066	0.283308	8				
135VSR	4.8 S	4.817	12.375	0.702164	0.513296	2.1022				0.02	0.03	6(1)
146ROV-2	4.8 S	4.806	12.378	0.702139	0.513299	2.1035	0.283302	8				
119DS-1	A0	6.273	11.376	0.702183	0.513321	2.1029	0.283348	9	5.42	0.05	0.04	3(1)
120DS-2	A0	6.399	11.338	0.702251	0.513275	2.0902			5.02	0.05	0.03	6(1)
121DS-1	A0	6.542	11.310	0.702203	0.513305	2.1018	0.283337	6				
126DS-2	AFZ	7.138	13.050	0.702136	0.513269	2.0933				0.03	0.02	3(1)
130DS-1	A1	7.584	13.470	0.702328	0.513332	2.0933	0.283365	7	5.45	0.04	0.04	3(1)
132DS-1	A1	7.666	13.456	0.702499	0.513138	2.0362	0.283229	6	5.22	0.05	0.04	6(1)
136DS-1	A1	7.773	13.432	0.702404	0.513166	2.0530			5.41	0.03	0.03	6(1)
138DS-1	A1	7.867	13.431	0.702699	0.513040	2.0077				0.09	0.00	3(1)
138DS-3	A1	7.867	13.431	0.702711	0.513038	2.0041	0.283097	7		0.09	0.03	3(1)
141DS-1	A1	7.986	13.431	0.702322	0.513275	2.0819	0.283320	4	5.46	0.05	0.01	3(1)
146DS-2	A1	8.167	13.446	0.702338	0.513187	2.0583			5.33	0.08	0.04	3(1)
153DS-2	A2	8.555	13.550	0.702462	0.513181	2.0353	0.283230	5				
162VSR	A2	8.770	13.511	0.702382	0.513254	2.0528	0.283379	8	5.54	0.04	0.04	6(1)
160VSR	A2	8.782	13.507	0.702491	0.513181	2.0284				0.08	0.02	5(1)
159ROV-4	A2	8.800	13.502	0.702469	0.513195	2.0325	0.283202	7				
159ROV-6	A2	8.797	13.503	0.702283	0.513190	2.0390			5.11	0.08	0.03	6(1)
159ROV-10	A2	8.791	13.503	0.702508	0.513159	2.0300	0.283157	7				
155ROV-1	A2	8.816	13.508	0.702386	0.513215	2.0242	0.283067	9				
155ROV-7	A2	8.817	13.500	0.702476	0.513207	2.0286			5.48	0.04	0.04	6(1)
160DS-1	A2	8.968	13.460	0.702357	0.513176	2.0242	0.283083	7				

160DS-2	A2	8.968	13.460	0.702354	0.513183	2.0251			5.25	0.03	0.04	6(1)
162DS-1	A2	9.080	13.445	0.702464	0.513149	2.0215				0.06	0.03	3(1)
166DS-4	A3	9.230	13.316	0.702670	0.513043	2.0277	0.283082	6				
203VSR	A3	9.545	13.211	0.702701	0.513043	2.0309	0.283108	7	5.25	0.11	0.03	5(1)
194ROV-7	A3	9.573	13.211	0.702692	0.513053	2.0288	0.283093	7				
190DS-4	A3	9.887	13.087	0.702701	0.513036	2.0296	0.283100	6		0.05	0.03	5(1)
191DS-3	A3	9.948	13.067	0.702670	0.513057	2.0320	0.283099	7				
194DS-1	A4	10.071	13.198	0.702523	0.513089	2.0443	0.283145	4	5.17	0.08	0.04	9(2)
195DS-2	A4	10.132	13.197	0.702442	0.513193	2.0641	0.283295	9		0.07	0.01	3(1)
196DS-3	A4	10.231	13.189	0.702614	0.513069	2.0397			5.58	0.10	0.03	3(1)
199DS-2	A4	10.484	13.170	0.702338	0.513252	2.0830			5.60	0.02	0.03	6(1)
200DS-1	A4	10.609	13.092	0.702434	0.513178	2.0626	0.283299	6				
201DS-5	A4	10.684	13.075	0.702564	0.513101	2.0232	0.283265	7	4.28	0.06	0.04	9(2)
202DS-1	A4	10.782	13.051	0.702382	0.513116	2.0545			5.44	0.08	0.04	9(2)
203DS-2	A4	10.882	13.038	0.702381	0.513191	2.0610	0.283312	6				
188ROV-4	A3 Ax. Smt.	9.708	13.080	0.702611	0.513041	2.0214			5.31	0.04	0.04	6(1)
175DS-2	A3 Smt. F	9.691	13.085	0.702522	0.513068	2.0329	0.283091	7				
176DS-2	A3 Smt. F	9.684	13.019	0.702731	0.513046	2.0302				0.06	0.04	9(2)
179DS-1	A3 Grattan	9.734	12.881	0.702641	0.513005	2.0158	0.283021	5		0.05	0.04	6(1)
183DS-3	A3 Smt. D	9.712	12.138	0.702617	0.513046	2.0180	0.283023	4	5.48	0.07	0.03	3(1)
BCR-2	USGS standard									0.08	0.03	4(1)
BCR-2*	USGS standard									0.06	0.06	6
BHVO-2	USGS standard									0.03	0.04	12(3)
BHVO-2*	USGS standard									0.02	0.03	6

N represents the total number of isotope analyses, and i represents the number of aliquots from different batches of column chemistry.

Sr-Nd-Pb data are from Hoernle et al. (2011). Within-run errors for $^{177}Hf/^{176}Hf$ are shown for the last significant digit. Full element data can be found in the Supplementary material.

*Published $\delta^{138/134}Ba$ values of BCR-2 and BHVO-2 (An et al., 2020).

Table 2

	A-DMM	Recycled AOC	ROC	UCC	GLOSS
Rb (ppm)	0.05	1.82	0.57	84	84
Sr (ppm)	7.66	68	81	320	302
Zr (ppm)	5.08	52	64	193	129
Nb (ppm)	0.15	1.2	2.0	12	9.4
Ba (ppm)	0.56	10.6	6.6	628	786
La (ppm)	0.19	0.8	1.7	31	29
Ce (ppm)	0.55	2.9	5.9	63	58
Sm (ppm)	0.24	1.8	2.7	4.7	6.0
Nd (ppm)	0.58	5.2	7.5	27	28
Th (ppm)	0.008	0.043	0.088	11	8.1
Pb (ppm)	0.018	0.05	0.09	17	21.2
$^{87}Sr/^{86}Sr$	0.7022	0.7037	0.7032	0.7160	0.7124
$^{143}Nd/^{144}Nd$	0.51330	0.51299	0.51306	0.51210	0.51221
$\delta^{138/134}Ba$ (‰)	0.03	0.25	0.14	0.00	0.02

A-DMM: average depleted mantle endmember (Workman and Hart, 2005), $\delta^{138/134}Ba$ value is set based on the most depleted MORB from this study.

Recycled AOC: Altered oceanic crust (Staudigel et al., 1996) modified during subduction (Kogiso et al., 1997) with Sr-Nd isotope composition signatures for a recycling age of 1 Ga. The $\delta^{138/134}Ba$ value is set based on published AOC data (Nan et al., 2017; Nielsen et al., 2018) and to fit the observed Ba isotope variations in MORB.

ROC: bulk recycled oceanic crust (Stracke et al., 2003) derived by mixing 25% AOC + 25% N-MORB + 50% gabbro (Stracke et al., 2003) with Sr-Nd isotope composition signatures for a recycling age of 1 Ga. The $\delta^{138/134}Ba$ values of AOC, N-MORB, and gabbro are chosen to be 0.25‰, 0.03‰, and 0.03‰ based on this work and previous studies to calculate the $\delta^{138/134}Ba$ of ROC.

UCC: upper continental crust with chemical composition from Rudnick and Gao (2014). $^{87}Sr/^{86}Sr$ and $^{143}Nd/^{144}Nd$ from Goldstein and Jacobsen (1988) and Chauvel et al. (2004), and $\delta^{138/134}Ba$ from Nan et al. (2018).

GLOSS: global subducted sediment as given by Plank and Langmuir (1998) and Plank (2014). The $\delta^{138/134}Ba$ value is estimated from the pelagic sediment average (Bridgestock et al., 2018; Nielsen et al., 2018, 2020).

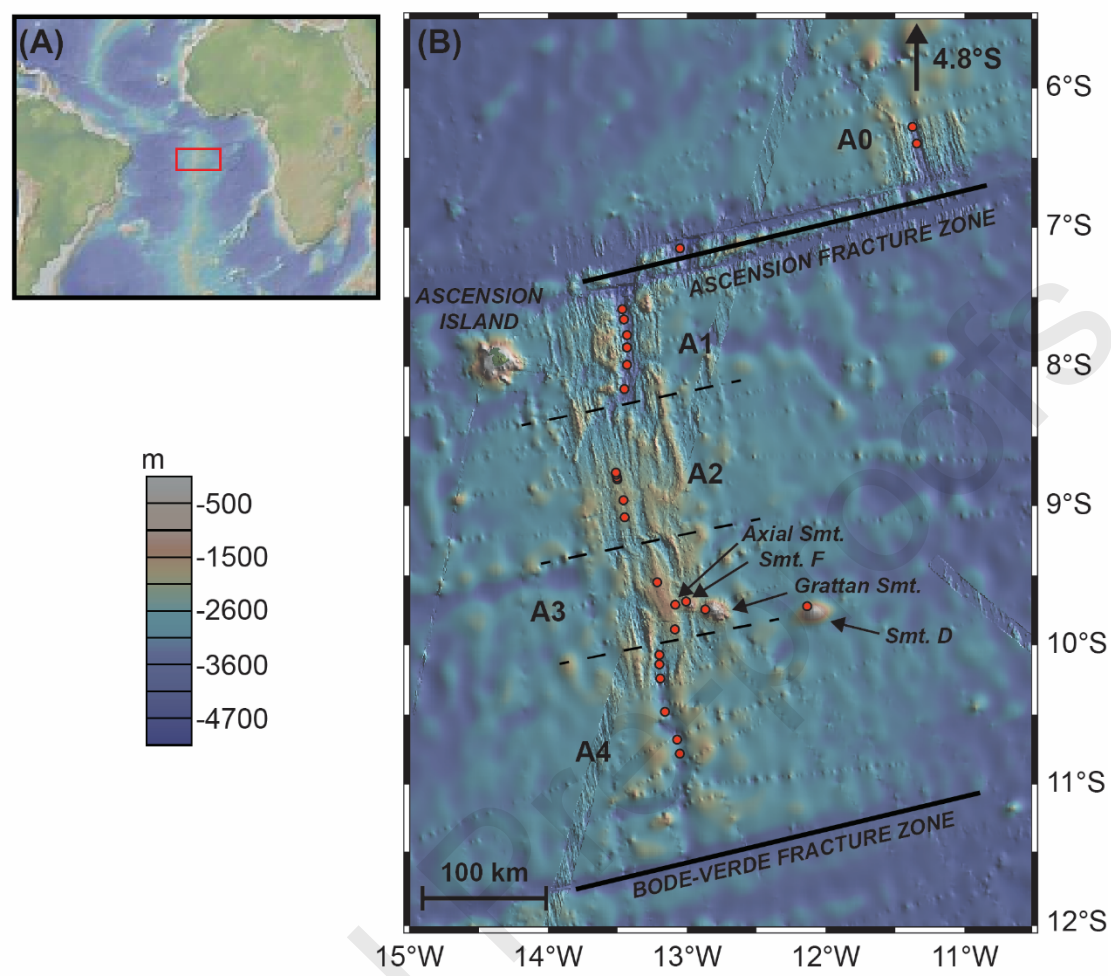

Figure 1 (A) The South Atlantic Mid-Ocean Ridge (SMAR) area between 5 and 11°S. (B) Overview bathymetric map showing the SMAR (5-11°S) just north of and between the Ascension Fracture Zone (AFZ) and the Bode Verde Fracture Zone (BVFZ). The SMAR can be divided into segment A0 on the north of the AFZ and segments A1 to A4 going from north to south between the AFZ and BVFZ. Also shown is Ascension Island adjacent to segment A1 and the off-axis A3 seamount chain (Axial, Seamount F, Grattan and Seamount D). The dredge locations for the samples studied are shown as filled red circles. Map is created using the GeoMapApplication tool (http://www.geomapapp.org, Ryan et al., 2009).

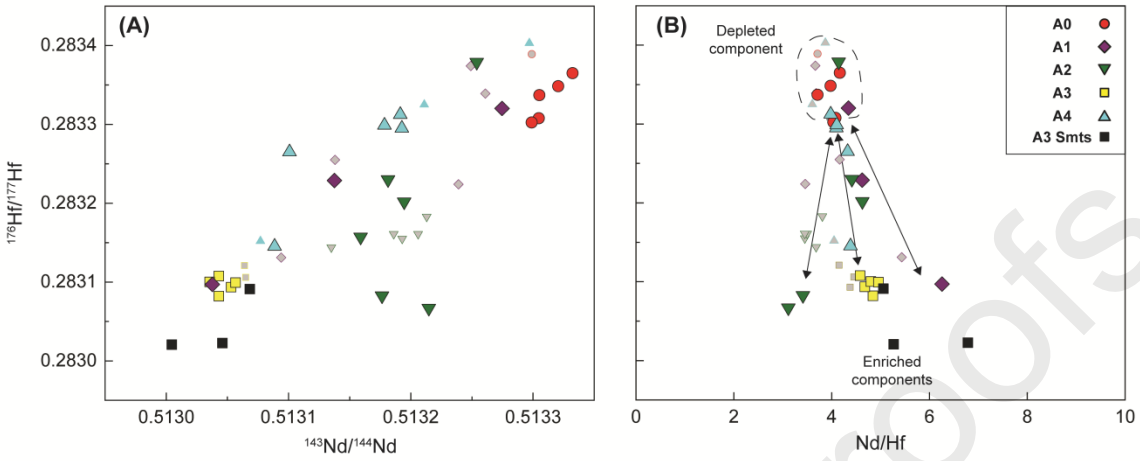

Figure 2 Plots of $^{176}Hf/^{177}Hf$ versus (A) $^{143}Nd/^{144}Nd$ and (B) Nd/Hf for the SMAR basalts. This figure shows that multiple enriched components are required to explain the observed range in geochemical compositions, as previously advocated by Hoernle et al. (2011). The colored symbols denote the samples studied in this study. The gray symbols denote the data presented by Paulick et al. (2010).

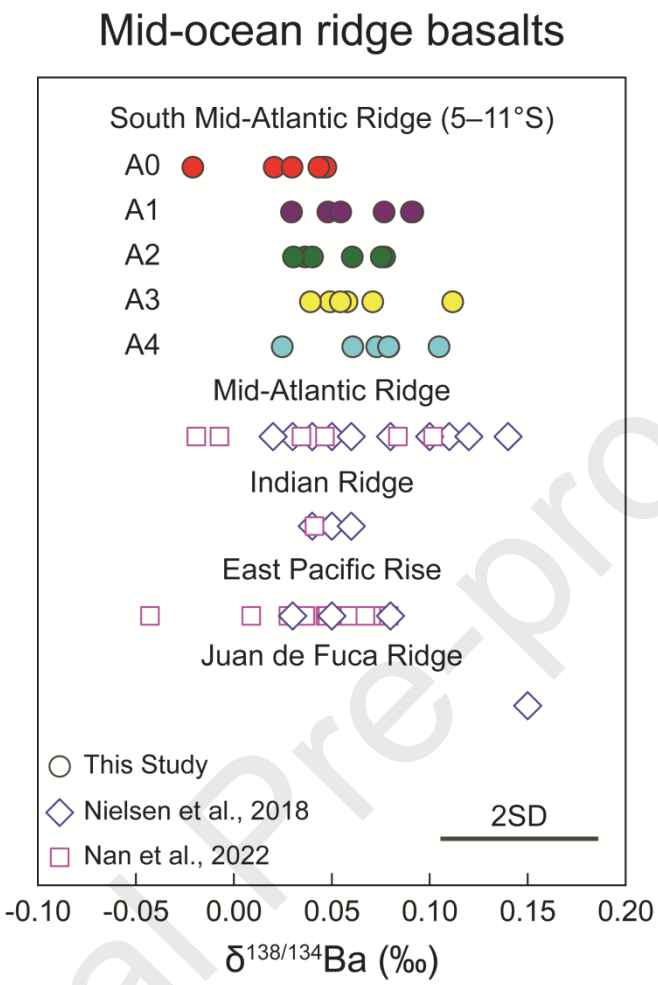

Figure 3. Ba isotope variations in mid-ocean ridge basalts. Data sources: this study, Nielsen et al., (2018) and Nan et al., (2022).

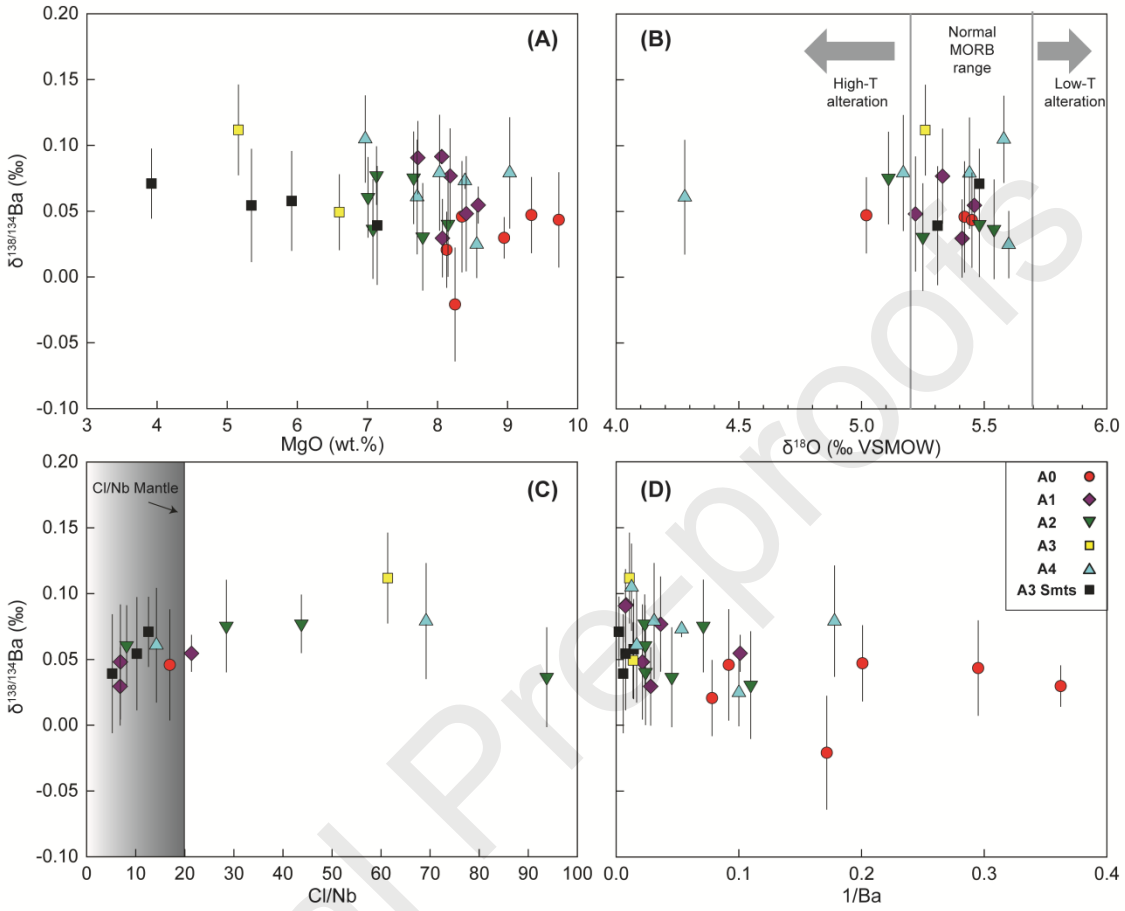

Figure 4 Plot of $\delta^{138/134}$Ba versus (A) MgO, (B) δ^{18}O, (C) Cl/Nb, and (D) 1/Ba of the SMAR basalt glasses. Also shown in (B) is the range of δ^{18}O values for pristine MORB from Eiler (2001) as well as potential modification trends. The Cl content data are from Turner er al. (2015). This figure shows that Ba isotope variations in these MORB samples could not be explained by magma differentiation or crustal assimilation.

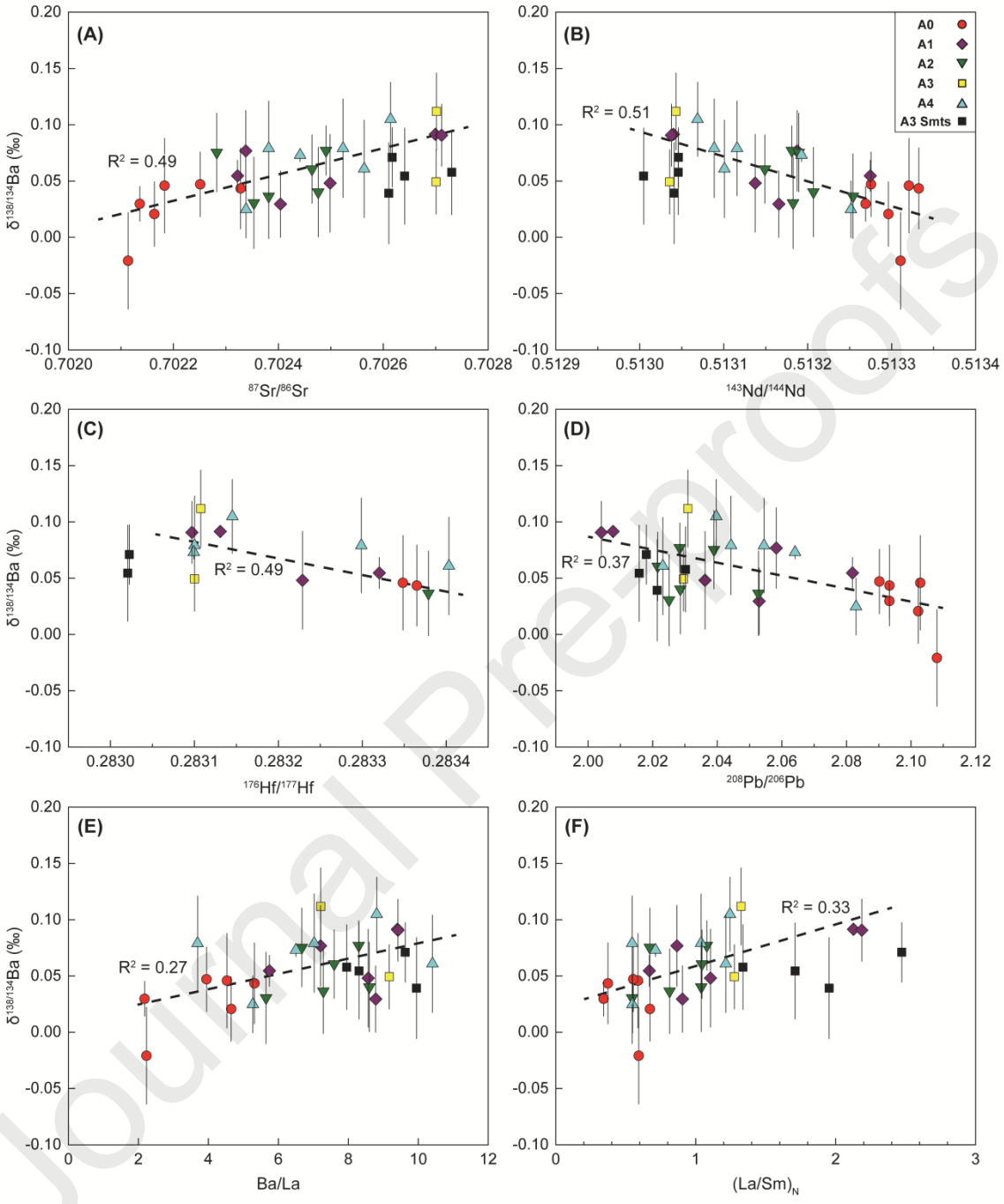

Figure 5 Plots of $\delta^{138/134}$Ba versus (A) $^{87}Sr/^{86}Sr$, (B) $^{143}Nd/^{144}Nd$, (C) $^{176}Hf/^{177}Hf$, (D) $^{208}Pb/^{206}Pb$, (E) Ba/La, and (F) $(La/Sm)_N$ for the SMAR basalts. Moderate correlations likely exist between Ba isotopes and radiogenic isotopes and trace element indicators of enriched components.

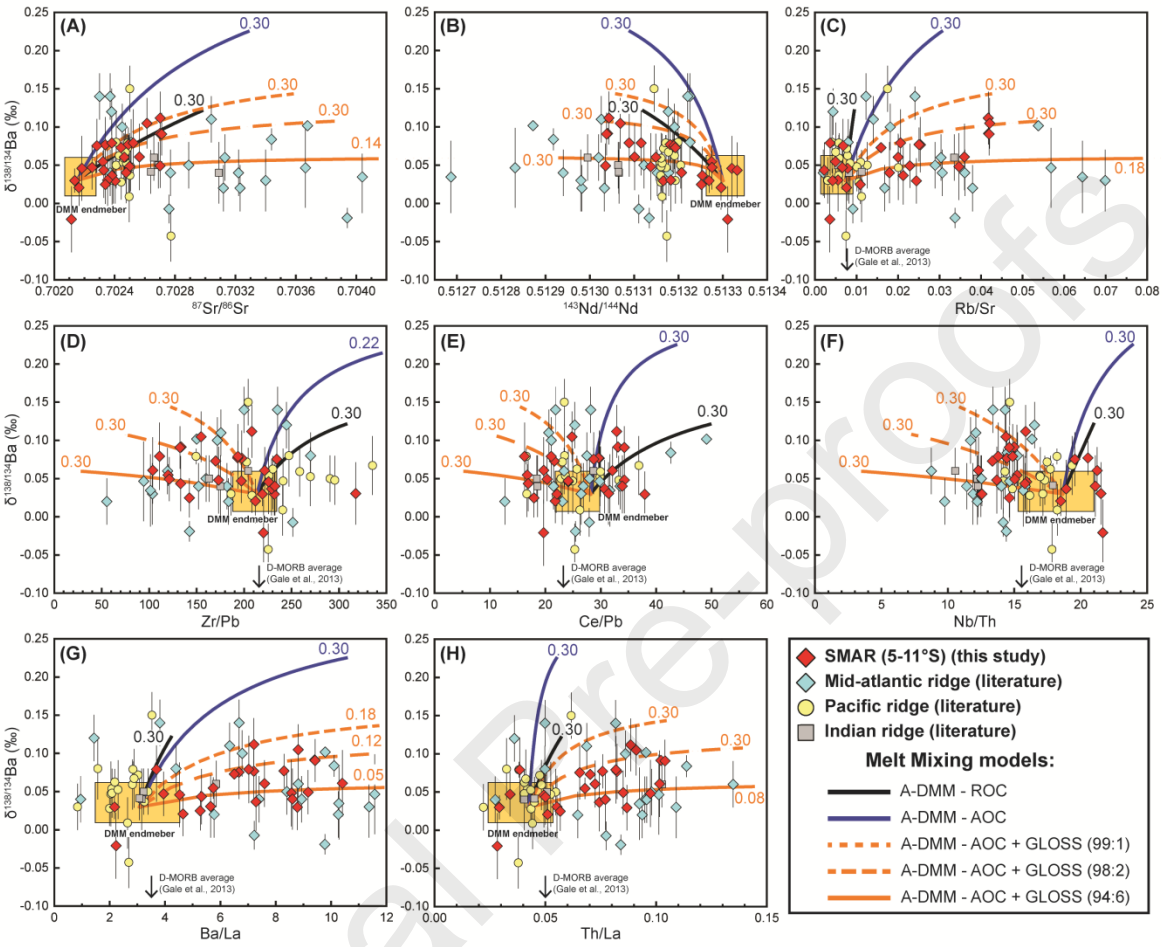

Figure 6 Variations between selected isotopic and elemental tracers and $\delta^{138/134}$Ba for MORB compared with modeled predictions for mixing of various source components: (A) $^{87}Sr/^{86}Sr$, (B) $^{143}Nd/^{144}Nd$, (C) Rb/Sr, (D) Zr/Pb, (E) Ce/Pb, (F) Nb/Th, (G) Ba/La and (H) Th/La. Modeling of melting and mixing between recycled materials and depleted mantle are made and shown in Figure 6 and Figure 7. The D-MORB melt endmembers are calculated by 10% model melting of peridotite with average DMM (A-DMM) compositions from Workman and Hart (2005). The melt endmembers are calculated by 10% model melting of pyroxenite with a composition of recycled altered oceanic crust (AOC) (blue) and a mixture of recycled AOC and subducted marine sediments (GLOSS) with mixing ratios of 99:1, 98:2 and 94:6 (orange). Also shown is the mixing of melt from A-DMM and the bulk recycled oceanic crust (ROC) (black) proposed by Stracke et al. (2003). The endmember

compositions are summarized in Table 2. The recycling age of the recycled component is assumed to be 1 Ga to calculate the Sr-Nd isotopes. The bulk partition parameters for peridotite and pyroxenite melting of elements are used after those compiled by Stracke and Bourdon (2009). The maximum proportion (0.05 to 0.30) of the assumed recycled component is denoted on the relevant mixing line. The arrows indicate the average elemental ratios of D-MORB estimated by Gale et al. (2013). Literature data are from Nielsen et al. (2018) and Nan et al. (2022). This figure shows that both recycled AOC and sediment components are required to explain the Ba isotope as well as other geochemical variations observed in MORB.

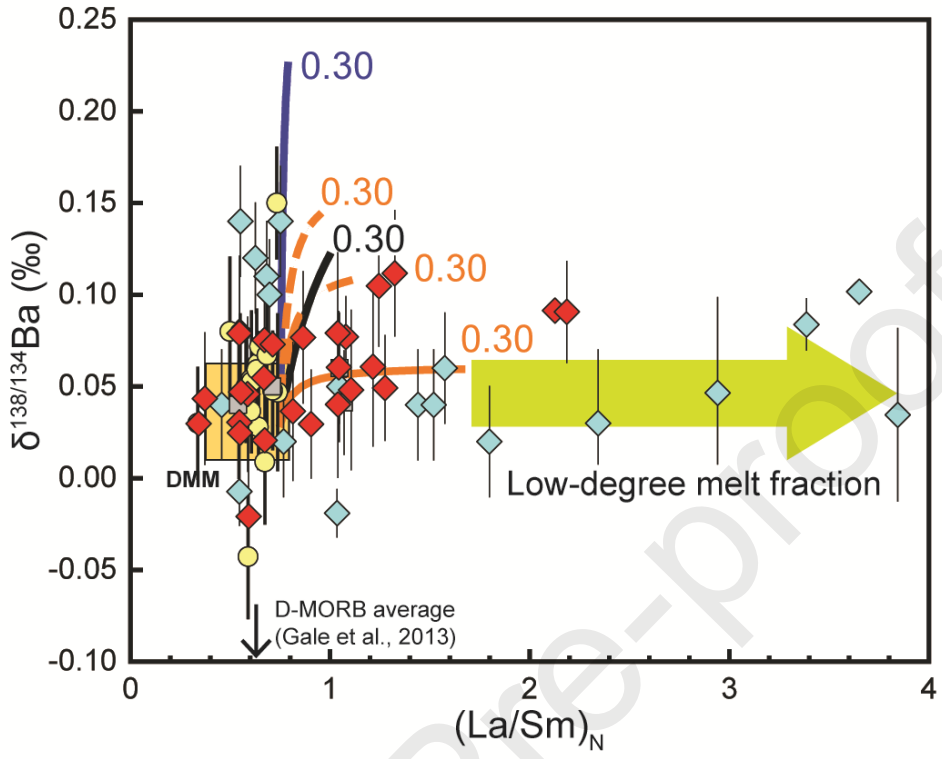

Figure 7 Correlations between $(La/Sm)_N$ and $\delta^{138/134}Ba$ values of MORB compared with predictions of various mixing models. The symbols and mixing models are the same as those used in Figure 6. This figure shows that the addition of low-degree melts is required to explain some MORB with elevated La/Sm ratios.

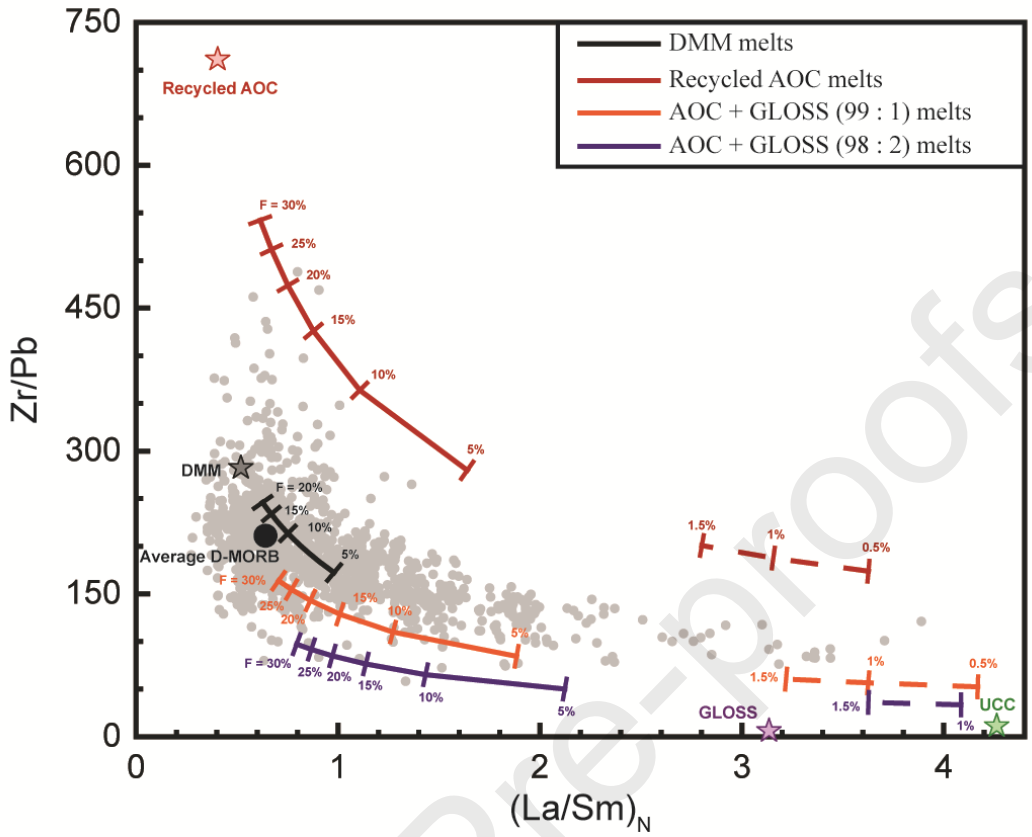

Figure 8 Correlations between $(La/Sm)_N$ and Ce/Pb values of global MORB compared with predictions of various melting models. The melting models and element partition parameters as complied by Stracke and Bourdon (2009) are used to calculate the variations in Zr/Pb and $(La/Sm)_N$ ratios in modeled melts. The peridotite melting model for the DMM (Workman and Hart, 2005) with melting fractions from 5 to 20% is shown as black line. The pyroxenite melting models of recycled AOC (red line), AOC + GLOSS (99 : 1, orange line), and AOC + GLOSS (98 : 2, purple line) with melting fractions from 5 to 30% and from 0.5 to 1.5% are shown with solid and dashed lines, respectively (Stracke and Bourdon, 2009; Plank, 2014; Rudnick and Gao, 2014). Data source of MORB: Jenner and O'Neill, 2012; Gale et al., 2013; Yang et al., 2018. This figure shows that mixing between the melts from DMM and low degree melts (F < 1.5%) from recycled components could not explain the observed high Zr/Pb ratio of quite a bit of MORB samples.

Declaration of interests

☒ The authors declare that they have no known competing financial interests or personal relationships that could have appeared to influence the work reported in this paper.

☐The authors declare the following financial interests/personal relationships which may be considered as potential competing interests: